Geomorphology 438 (2023) 108805

Contents lists available at ScienceDirect

Geomorphology

journal homepage: www.journals.elsevier.com/geomorphology

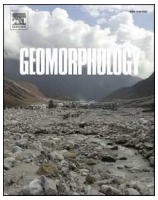

# Multi-decadal erosion rates from glacierized watersheds on Mount Baker, Washington, USA, reveal topographic, climatic, and lithologic controls on sediment yields

Eli Schwat [a,*], Erkan Istanbulluoglu [a], Alexander Horner-Devine [a], Scott Anderson [b], Friedrich Knuth [a], David Shean [a]

[a] Department of Civil and Environmental Engineering, University of Washington, Seattle, WA, USA
[b] U.S. Geological Survey, Washington Water Science Center, Tacoma, WA, USA

ARTICLE INFO

*Keywords:*
Glacier retreat
Debris flow
Sediment yield
Hazards
Sedimentation
Flooding
Cascade volcanoes
Climate change

ABSTRACT

Understanding land surface change in and sediment export out of proglacial landscapes is critical for understanding geohazard and flood risks over engineering timescales and characterizing landscape evolution over geomorphic timescales. We used automated Structure from Motion software to process historical aerial photographs and, with modern lidar data, generated a high-resolution DEM time series with coverage over 10 glacierized watersheds on Mount Baker, Washington, USA for the time period between 1947 and 2015. We measured basin-wide sediment yields and sediment redistribution on hillslopes and in stream channels. Slopes within most measured erosion sites are above theoretical and observed debris-flow thresholds. We observed significant erosion of hillslopes and limited deposition on hillslopes and in stream channels. Sediment delivery ratios during time periods with net erosion averaged 0.73. We determined, consistent with previous field observations, that debris flows originating from moraines are a primary erosion mechanism in proglacial zones on Mount Baker. Time series measurements indicate that temporal variability in erosion rates is associated with climate oscillations, with higher erosion rates during cooler-wetter periods. Basin-wide sediment yield is positively correlated with lithology ($r^2 = 0.54$), hillslope angle ($r^2 = 0.52$), drainage area ($r^2 = 0.82$), and negatively correlated with stream channel slope ($r^2 = 0.67$). Topographic differences between high and low yielding basins indicate that spatial variability in erosion on Mount Baker is sensitive to Pleistocene and Holocene glacial and volcanic activity. Specific sediment yields in six basins averaged 4600 ton/km$^2$/yr, consistent with global measurements in glacierized catchments. Specific sediment yield decreased with increasing basin area, with total loads in the downstream main stem Nooksack River estimated between 480 and 820 ton/km$^2$/yr. Proglacial sediment yields account for between 18 and 32 % of total sediment load in the main stem Nooksack River and exceed contributions by bluff and terrace erosion, which account for between 8 and 13 % of total load. Our findings indicate that erosion in glacierized basins is sensitive to decadal climate oscillations and that high proglacial sediment yields provide an important contribution to river systems downstream, particularly in catchments where upland topography and lithology is favorable.

## 1. Introduction

Glacier advance and retreat increase erosion and sediment yields within proglacial zones, areas between the moraines of the latest glacial maximum and the upstream, retreated active glacier margin (e.g., Antoniazza and Lane, 2021). Since the Last Glacial Maximum (LGM) (~20 ka BP), geologic records reveal several epochs of glacier readvance and retreat as a result of climate variability. The most recent and profound glacier readvance was the Little Ice Age (LIA) (ca. 1300–1850). Terminus positions of mountain and arctic glaciers have retreated rapidly from their mid-19th century LIA maximum, making proglacial zones among the most rapidly changing landscapes measured globally to date (Carrivick and Heckmann, 2017).

Proglacial zones are transient systems, moving from a geomorphic equilibrium constructed during the last major glaciation, with characteristic relict structures and deposits (hanging valleys, steep moraine

* Corresponding author.
*E-mail address:* elilouis@uw.edu (E. Schwat).

https://doi.org/10.1016/j.geomorph.2023.108805
Received 13 January 2023; Received in revised form 20 June 2023; Accepted 21 June 2023
Available online 30 June 2023

terraces, and rock walls), to a new equilibrium of non-glacial conditions, with snowmelt and rain-driven geomorphic processes dominance (e.g., Legg et al., 2014; Lane et al., 2017). According to the conceptual model of Antoniazza and Lane (2021), modern sediment yields of glacierized alpine watersheds still reflect early phases of LIA paraglacial adjustment, together with the legacy of LGM landforms and deposits. During paraglacial adjustment, glacier retreat debuttresses over-steepened moraines, intense rainstorms and prolonged wet periods initiate landslides and debris flows, and drainage networks expand upslope, increasing catchment-scale sediment connectivity (Lancaster et al., 2012; Legg et al., 2014; Carrivick and Heckmann, 2017; Lane et al., 2017). At the river basin scale, disequilibrium sediment yields may continue over much longer time frames, as river networks downstream of upland proglacial areas incise through and remobilize LGM glacial deposits in valley floors (e.g., Church and Slaymaker, 1989).

Studies of multiple proglacial basins reveal that sediment export rates vary tremendously in relation to lithology, characteristics of relict topography, tectonic activity, and changing hydrologic conditions (Holm et al., 2004; Carrivick and Rushmer, 2009; Carrivick and Heckmann, 2017; Carrivick and Tweed, 2021). Yields in proglacial basins may also vary in response to anthropogenic warming. Both warming and glacier mass losses have accelerated since the 1980s (Zemp et al., 2015; Frans et al., 2018; Hugonnet et al., 2021) and it is expected that warming and associated extreme precipitation events will increase proglacial erosion rates (Carrivick and Tweed, 2021).

Proglacial and upland sediment yield variation over engineering timescales may pose flood risk downstream. A common adage regarding river systems with headwaters in steep glacierized mountains (e.g., the Cascade Range and Coast Mountains of North America) is that the uplands are constantly shedding sediments that fill riverbeds downstream. Studies show that channel aggradation, rather than elevated streamflow, may be responsible for flood events (Slater et al., 2015; Ahrendt et al., 2022), and that variation in proglacial sediment yields and downstream channel aggradation may be linked (Anderson and Konrad, 2019; Pfeiffer et al., 2019). However, the relative contribution of proglacial sediments to river basin scale sediment budgets remains unclear.

The behavior of proglacial and steep mountain landscape erosion processes and sediment yields over decadal timescales remains poorly understood, in part because field study of these environments must take place at rugged and remote sites. Sediment cores from marine and lake deposits and seismic sensing methods provide evidence for changes in sediment yields from mountains with retreating glaciers over millennial to centennial timescales (e.g., Elverhøi et al., 1998; Hasholt et al., 2000). Modern records, including stream gage measurements and high-resolution topographic datasets (e.g., airborne lidar and Structure from Motion (SfM) photogrammetry), show high sediment yields in deglaciating watersheds over decadal to interannual timescales (e.g., Bogen, 2008; Koppes and Montgomery, 2009; Czuba et al., 2012; Anderson and Pitlick, 2014; Micheletti et al., 2015; Anderson et al., 2019). The increased availability of high-resolution topographic datasets is allowing study over sub-decadal timescales, in settings where field measurements were previously difficult or impossible (Lancaster et al., 2012; Anderson and Pitlick, 2014; Legg et al., 2014; Mancini and Lane, 2020; Anderson and Shean, 2022; Betz-Nutz et al., 2023).

Answering the following research questions is critical to improve our understanding of steep-slope erosion mechanisms, paraglacial adjustment, upland sediment yields, and their impact on flood risk:

1. Which topographic factors control the magnitude and spatial variability of erosion rates and sediment yields in proglacial basins?
2. How do sediment yields vary in time in relation to climatic trends?
3. What is the relative contribution of proglacial sediments at the river basin scale?

We study these questions by measuring and comparing multi-decadal erosion rates in ten proglacial catchments on Mount Baker in Washington State (WA), USA, using a high-resolution Digital Elevation Model (DEM) time series that spans the years 1947–2015.

## 2. Study area

Mount Baker (indigenous name, Koma Kulshan) is an active, andesitic stratovolcano in the Cascade Volcanic Arc with a summit elevation of 3286 m (Wood and Kienle, 1990). Among the proglacial catchments we studied, Deming, Thunder, Coleman, Roosevelt, and Mazama Glacier valleys on Mount Baker feed into the undammed North and Middle Forks of the Nooksack River, which flows west and empties into the Bellingham Bay (Fig. 1). The remaining watersheds feed into the man-made Baker Lake and Lake Shannon reservoirs to the southeast, both part of the Skagit River watershed. The Nooksack River has a history of managed dredging operations and, by some estimates, carries the largest specific sediment yield (SSY) of major Puget Sound rivers (Anderson et al., 2019). Recent flooding of the Nooksack in November 2021 cost approximately $50 million in Washington State alone (Associated press, 2021). During this event, the Nooksack River overtopped its banks in Everson, WA, and flowed into the Sumas River, across the international border to Abbotsford, British Columbia. Economic costs associated with this flooding in British Columbia exceeded $1 billion (Dalton, 2021). Recent studies in the Nooksack River have linked proglacial erosion with downstream aggradation (Anderson and Konrad, 2019).

Mount Baker is the second most glacierized volcano in Washington state after Mount Rainier, with approximately 38.6 $km^2$ of area covered by glaciers (Pelto and Brown, 2012). Mount Baker's glaciers have generally been retreating since the end of the LIA (Dick, 2013). Large lateral moraines identify glacier extent during their LIA maxima (Fig. 1). In response to regional climate forcing, glaciers rapidly retreated between 1930 and 1945, advanced between 1945 and 1980, and most have been retreating since 1980 (Harper, 1993; Dick, 2013). Frans et al. (2018) estimate that glaciers on Mount Baker, relative to their 1960 extents, will decrease in area between 50 and 100 % by 2100.

Mount Baker and much of the surrounding area was covered by an ice sheet during the Fraser Glaciation (34–11.6 ka). The volcano has experienced multiple eruptive periods since, one as recently as the mid-1800s (Scott et al., 2020). The surface lithology of Mount Baker is composed primarily of Holocene-Pleistocene and Quaternary (igneous) andesite flows, Cretaceous-Jurassic marine sedimentary bedrock, and Pleistocene glacial till and drift (Fig. S3, S4) (Tabor et al., 2003). Modern observations on Mount Baker have identified debris flows as an important sediment transport mechanism (Fuller, 1980; Tucker et al., 2014). A 10 million $m^3$ debris flow in June 1927 originated near the Deming Glacier terminus, and two events of similar size that occurred between 1860 and 1890 originated near the Rainbow Glacier (Table S7) (Fuller, 1980; Tucker et al., 2014; Scott et al., 2020). More recently, two approximately 100,000 $m^3$ debris flows originated from the Deming Glacier basin in May and June of 2013 (Tucker et al., 2014). Field observations indicated that the deposits from these events mostly eroded within three weeks, suggesting that similarly sized debris flows may erode beyond recognition within a few years (Tucker et al., 2014).

## 3. Methods

To address our research questions, we produced a DEM time series with coverage over Mount Baker and measured glacier changes, local erosion, watershed sediment yield, and terrain characteristics in ten distinct watersheds. We then produced a sediment budget for the Nooksack River using our measurements and measurements from the literature.

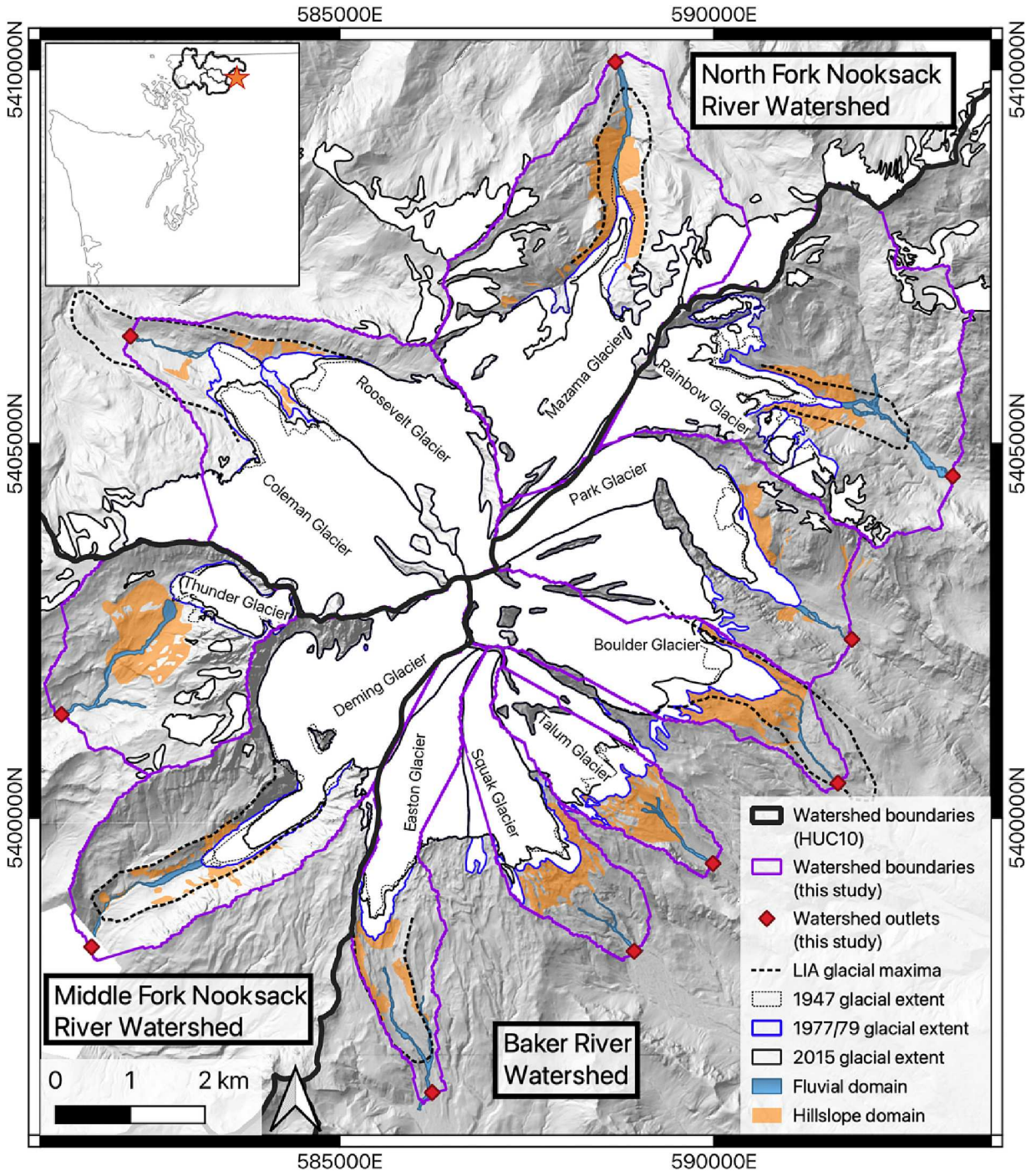


**Fig. 1.** Context map for Mount Baker glaciers and watersheds overlaid on a hillshade generated from a 2015 US Geological Survey lidar DEM. The Little Ice Age (LIA) glacial maxima are from Roe and O'Neal (2009), except for Mazama Glacier, which is inferred from topography. Other LIA extents are not presented in the literature and are not identifiable from topography. Glacier extent, modified from the Randolph Glacier Inventory (RGI) (RGI Consortium, 2017), is shown for all named glaciers in 1947, 1979 and 2015; for Rainbow Glacier, the 1977 glacier boundary is shown instead of 1979. For unnamed glaciers and perennial snowfields, the unmodified RGI outlines are shown. Fluvial and hillslope domains are manually delineated. HUC10 watershed boundaries are from the NHDPlus database. The inset figure shows the location of Mount Baker (star) and the Nooksack River watershed and its three forks within the Puget Sound region of Washington State.

### *3.1. Preparing DEMs, orthomosaics, and DEMs of difference*

#### *3.1.1. Historical aerial photographs*

We downloaded scanned historical aerial photographs taken in 1947 from the US Geological Survey (USGS) Aerial Photo Single Frame dataset (Earth Resources Observation and Science (EROS) Center, 2017) available from the USGS EarthExplorer data portal (EE). The 1947 photographs were collected in an overlapping grid pattern from an altitude of approximately 6000 m, providing complete coverage of Mount Baker with an average ground sample distance of one meter. We also downloaded all available scanned photographs acquired between 1970 and 1992 over Mount Baker as part of the USGS North American Glacier Aerial Photography (NAGAP) program (Post et al., 1971; Post, 1995), from the NSF Arctic Data Center (Nolan et al., 2017). These images were captured from variable altitudes and have an average ground sample distance of 30 cm. The NAGAP imagery was generally

collected along single flight lines oriented parallel to glacier centerlines, with coverage over the lower glacier and forefield. All historical photographs were captured between August and October, when seasonal snowpack was minimal or nonexistent.

#### 3.1.2. Historical structure from motion (HSfM)

We followed the processing methodology outlined by Knuth et al. (2023) to derive DEMs and orthomosaics from the scanned historical aerial photographs. Scanned images were downloaded and standardized using the Historical Image Preprocessing (HIPP) software package (Knuth et al., 2021a). We then generated 2-meter DEMs using the Historical Structure from Motion (HSfM) software package (Knuth et al., 2021b). HSfM generates self-consistent and accurately geolocated DEMs and orthomosaics using a reference DEM and a robust, multi-stage DEM co-registration process, without manually derived ground control (Knuth et al., 2023). For the reference DEM, we used a 1-meter Digital Surface Model (DSM) derived from an airborne laser scanning survey completed between August and September 2015. This data was obtained from the Washington Department of Natural Resources (WADNR) lidar portal. We approximate the lidar collection date as September 1, 2015, throughout this study. Fig. 2 shows the nine DEMs generated using HSfM in this study, the 2015 lidar DEM, and which DEMs are used for measurements in each watershed (Section 3.3).

#### 3.1.3. Orthomosaic time series

In addition to DEMs, HSfM produces orthomosaics for each single-date collection of aerial photographs. We augmented the historical orthomosaic record with an aerial orthomosaic collected on September 28, 2015, as part of the National Agriculture Imagery Program (NAIP, retrieved from EE).

#### 3.1.4. DEM of difference time series

We map long-term, 68-year, geomorphic change across ten watersheds (referred to by the name of their glaciers, Fig. 1) by differencing the 1947 and 2015 DEMs to create a DEM of Difference (DoD) (Fig. 2). The DoD revealed that most geomorphic activity occurred within the Mazama, Rainbow, Deming, and Coleman proglacial zones during this period (Fig. S10). We created additional DoDs, one for each consecutive pair of DEMs (Fig. 2B), and performed further analysis on these four "high-erosion watersheds."

To create DoDs, we first resampled the 2015 lidar DSM, originally in a 1-meter grid, to a 2-meter grid. We then resampled all historical DEMs to match the 2-meter grid of the lidar DSM and subtracted the 2015 DEM from each historical DEM. A 2-meter grid offers a good compromise between detail and artifact mitigation. All resampling was performed using cubic interpolation. We performed two post-processing steps to improve DoD data quality. First, we removed outlier pixels with absolute elevation change values >50 m, the magnitude of the largest observed geomorphic change between 1947 and 2015. Elevation change signals larger than 50 m were caused by artifacts (e.g., scratches on the aerial photograph film). We found that measurements of volumetric change were not sensitive to this threshold when varied above ±50 m. Second, we interpolated across data gaps in the DoDs by applying a linear interpolation algorithm with a maximum lateral search distance of 50 m (Xdem Contributors, 2021), which is sufficient to fill all data gaps in the study areas. All DoDs used in this study are listed in Table 1.

### 3.2. Basin and measurement area definition

#### 3.2.1. Watershed boundaries

For each of the ten watersheds (Fig. 1), we manually identified

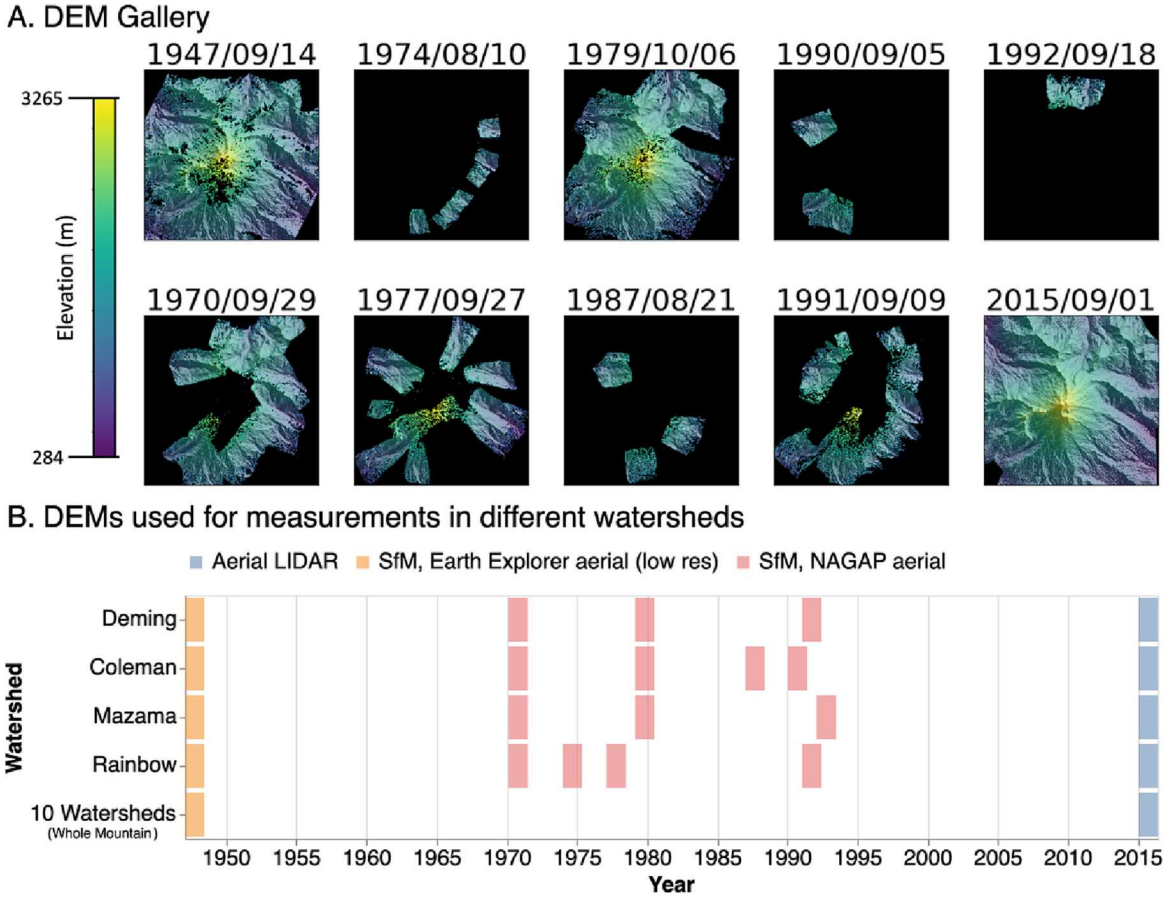


**Fig. 2.** (A) Gallery of colorized shaded relief maps for DEMs used in this study, showing spatial coverage for each available year. (B) Visualization of DEM temporal coverage for individual valleys and all of Mount Baker, with colors representing data source.

**Table 1**
Error statistics for all DEMs of Difference (DoDs) used in this study. Mean, RMSE, Range, Sill, and 90 % CI Lower/Upper bounds refer to the statistics calculated for all stable ground in each DoD (Section 3.4).

| Name | Start Date | End Date | Interval (years) | Mean (m) | RMSE (m) | Range (m) | Sill (m) | 90 % CI Lower Bound (m) | 90 % CI Upper Bound (m) |
|---|---|---|---|---|---|---|---|---|---|
| Coleman | 9/14/47 | 9/29/70 | 23 | 1.03 | 2.83 | 13.42 | 6.18 | −3.31 | 5.37 |
| Coleman | 9/29/70 | 10/6/79 | 9 | −0.67 | 1.36 | 9.62 | 1.14 | −2.62 | 1.29 |
| Coleman | 10/6/79 | 8/21/87 | 8 | −1.03 | 2.08 | 18.93 | 2.3 | −4.01 | 1.95 |
| Coleman | 8/21/87 | 9/5/90 | 3 | 1.5 | 2.54 | 18.43 | 1.45 | −1.88 | 4.87 |
| Coleman | 9/5/90 | 9/1/15 | 25 | −0.22 | 1.11 | 48.12 | 1.37 | −2.01 | 1.57 |
| Coleman | 9/14/47 | 9/1/15 | 68 | 0.47 | 1.95 | 26.25 | 2.14 | −2.64 | 3.59 |
| Rainbow | 9/14/47 | 9/29/70 | 23 | −0.57 | 1.89 | 8.9 | 2.74 | −3.54 | 2.4 |
| Rainbow | 9/29/70 | 8/10/74 | 4 | −0.33 | 0.92 | 15.91 | 0.69 | −1.74 | 1.09 |
| Rainbow | 8/10/74 | 9/27/77 | 3 | 0.11 | 0.66 | 15.74 | 0.41 | −0.96 | 1.18 |
| Rainbow | 9/27/77 | 9/9/91 | 14 | 0.06 | 0.6 | 8.66 | 0.34 | −0.92 | 1.04 |
| Rainbow | 9/9/91 | 9/1/15 | 24 | −0.07 | 0.48 | 6.86 | 0.23 | −0.86 | 0.72 |
| Rainbow | 9/14/47 | 9/1/15 | 68 | −0.78 | 2.02 | 7.92 | 3.12 | −3.85 | 2.28 |
| Mazama | 9/14/47 | 9/29/70 | 23 | 1.12 | 2.48 | 29.72 | 4.21 | −2.52 | 4.76 |
| Mazama | 9/29/70 | 10/6/79 | 9 | 0.09 | 0.76 | 22.56 | 0.45 | −1.14 | 1.32 |
| Mazama | 10/6/79 | 9/18/92 | 13 | −0.31 | 1.28 | 65.27 | 1.26 | −2.35 | 1.72 |
| Mazama | 9/18/92 | 9/1/15 | 23 | 0.14 | 1.36 | 101.91 | 1.47 | −2.08 | 2.36 |
| Mazama | 9/14/47 | 9/1/15 | 68 | 0.85 | 2.65 | 38.17 | 5.91 | −3.28 | 4.98 |
| Deming | 9/14/47 | 9/29/70 | 23 | −0.45 | 1.32 | 15.02 | 1.53 | −2.49 | 1.59 |
| Deming | 9/29/70 | 10/6/79 | 9 | 0.54 | 0.91 | 2.39 | 0.14 | −0.65 | 1.74 |
| Deming | 10/6/79 | 9/9/91 | 12 | −0.03 | 0.71 | 23.07 | 0.43 | −1.21 | 1.14 |
| Deming | 9/9/91 | 9/1/15 | 24 | −0.18 | 0.76 | 26.18 | 0.47 | −1.4 | 1.03 |
| Deming | 9/14/47 | 9/1/15 | 68 | 0.7 | 1.34 | 26.24 | 1.24 | −1.18 | 2.57 |
| Whole mountain | 9/14/47 | 9/1/15 | 68 | 0.49 | 2.25 | 68.55 | 3.79 | −3.11 | 4.1 |

watershed outlet points where stream channels cross the downstream extent of the 1947 DEM coverage (Fig. 2A). We automatically delineated watershed boundaries upstream of the outlet points with D8 flow direction and flow accumulation algorithms implemented in the StreamStats web tool (Fig. 1) (U.S. Geological Survey, 2019). The watershed containing both Coleman and Roosevelt Glaciers is hereinafter referred to as the Coleman watershed.

#### 3.2.2. Glacier polygons

We delineated glacier outlines throughout our study time period by modifying polygons from the Randolph Glacier Inventory (RGI Consortium, 2017). For each of the 11 studied glaciers (Fig. 1) and for each DEM timestamp with coverage over that glacier (Fig. 2), we manually modified the original RGI polygon to outline the glacier extent apparent in the DEM and orthomosaic. DoDs aided identification of glacier boundaries where debris-cover rendered the glacier extent difficult to identify with imagery. Glacier boundaries are easily identified in DoDs, which show large, widespread elevation change where glaciers advanced or retreated.

#### 3.2.3. Delineation of measurement areas for change detection

To measure volumetric change, we manually delineated bare ground areas with repeated DEM coverage in ten watersheds (Fig. 2). Bare ground area is defined as areas that are unvegetated through the entire study period or areas that were bare in 1947, eroded, and then grew vegetation. Our DEM time series has different extent and coverage in each year due to the inconsistent coverage of the historical photographs used for SfM reconstruction (Fig. 2A). Thus, we exclude many areas where we cannot quantify changes with multiple DoDs from measurement. Areas with snow cover during any date in our DEM time series are also excluded.

To track the movement of sediment from hillslopes to stream channels, we split the delineated bare ground area into a hillslope and a fluvial domain (Figs. 1 and 2). We visually examined orthomosaics and a slope raster (Section 3.5) to manually outline each watershed's primary stream channel, extending from the 2015 glacier terminus to the watershed outlet point (Fig. 1). Fluvial domains map the stream channel from bank to bank, with banks identified by sudden increases in slope or a vegetation boundary. Hillslope domains include all bare ground areas that are not within the fluvial domains.

To examine eroded sediment source areas, we manually delineated erosion sites in the four high-erosion watersheds (Section 3.1.4). Each erosion polygon outlines an area with negative land surface change that appears to be due to a single erosion event (e.g., a landslide scar) or repeated erosion events that deepen an eroded area (e.g., a gully). The erosion polygons delineate all areas within the bare ground area that eroded during our measurement time period, while the bare ground area includes eroded land, land on which deposition occurred, and stable land.

We acknowledge that identifying debris-covered ice in historical orthomosaics is challenging. It is possible to mistake the melt out of "dead ice," which we define as ice buried beneath debris and discontiguous from a nearby glacier, for erosion. We excluded from measurement any areas where the intermixing of sediment signals with surface lowering due to ablation of ice was judged to be likely.

### 3.3. Measuring volumetric change and sediment yield

For the ten watersheds, we measured long-term net volumetric change within the bare ground area (the combined hillslope and fluvial domains) using the 1947–2015 DoD (Fig. 2B, S10). In the four high-erosion watersheds, we measured net and gross positive and negative volumetric changes separately in the hillslope and fluvial domains using the time series of DoDs available in each watershed (Fig. 2B).

We calculated net volumetric change as the sum of all DoD pixels in a given area multiplied by pixel area (2-m x 2-m, Section 3.1.4) and gross positive/negative change as the sum of all positive/negative DoD pixels in a given area multiplied by pixel area. For gross change measurements, DoD values are thresholded at the 90 % confidence level (Section 3.4) (Anderson, 2019; Anderson and Shean, 2022). When making all measurements, we excluded glacier change signals by removing pixels within the glacier outlines associated with the beginning and end dates of the DoD (Section 3.1.4).

The measurements of net volumetric change in ten watersheds provide estimates of net sediment export (Carrivick and Tweed, 2021). For comparison with other studies, we convert net volumetric change ($\Delta V$) to sediment yield ($SY$) in units of metric tons. To calculate SY, we first converted ($\Delta V$) from a bulk volume to a rock volume with an estimate of morainic porosity, $n = 0.35$ (Humlum, 2000; Burki et al., 2010), because most observed erosion occurred on moraines. We then convert to SY in

units of mass using the approximate density of andesite, $\rho_{rock} = 2600$ kg/m$^3$ (Klein and Johnson, 1983, Werner et al., 2009),

$$SY = -\Delta V(1-n)\rho_{rock} \quad (1)$$

While the surface lithology of Mount Baker is heterogeneous, we use a single andesite density value for all measurements, because the volcano is an andesitic cone (Scott et al., 2020), andesite flows are the primary surface lithology in our measurement areas (Fig. S3), and we lack information about the lithological composition of moraines. Note that $SY$ is proportional to negative $\Delta V$ (Eq. (1)) because negative net volumetric change indicates erosion without compensating deposition, and therefore export of material from the measured area.

Our volume change and sediment yield measurements account for storage changes in a limited subset of bare ground areas in each watershed. We cannot quantify storage changes within the entire watershed due to glacier and vegetation cover and the limited spatial coverage of various DEMs in our time series (Fig. 2). We also cannot quantify supra- or subglacial sediment change.. Because of these limitations, we cannot completely close the watershed sediment mass balance and in some watersheds, we measure positive net volumetric change which results in negative sediment yield (Eq. (1)). Negative sediment yield measurements in our study do not indicate an erroneous result—we still assume that watershed boundaries act as zero-flux boundaries for sediment—they simply indicate that we could not measure all the sediment changes occurring across the watershed due to the data limitations discussed above. In watersheds with positive sediment yield, our measurements likely represent minimum estimates of the total sediment flux passing the watershed outlets.

We use a relative sediment balance index (RSI), the ratio between net volumetric change ($\Delta V$) and gross negative volumetric change (ie., gross erosion, $\Delta V^-$, where $\Delta V^- \leq 0$),

$$RSI = \Delta V / \Delta V^-, \quad (2)$$

as a way to measure how sediment export from a watershed compares to erosion within the watershed. RSI is similar to the sediment delivery ratio, a common index used in engineering calculations, except that sediment delivery ratio generally uses sediment yield measurements at a watershed outlet, which are always positive, while in our measurements, sediment yield can be negative. $\Delta V^-$ is always negative, thus RSI is positive when there is net sediment export from a watershed ($\Delta V < 0$) and negative when there is net deposition within a watershed ($\Delta V > 0$) (Eq. (1)).

### 3.4. Uncertainty estimation

Using the DoDs (Section 3.1.4), we measured volume changes (Section 3.3) within delineated areas (Section 3.2). To estimate the uncertainty associated with these measurements, we use an error model for volumetric uncertainty, $\boldsymbol{\sigma}_v$, that incorporates the random errors, systematic errors, and spatially correlated errors present in the DoD,

$$\sigma_v = nL^2\sqrt{\frac{\sigma_{rms}^2}{n} + \frac{\sigma_{sc}^2}{n}\frac{\pi a_i^2}{5L^2} + \sigma_{sys}^2}, \quad (3)$$

where $n$ is the number of pixels in a measurement, $L$ is the DoD resolution (2 m), and $\boldsymbol{\sigma}_{rms}$ and $\boldsymbol{\sigma}_{sys}$ are the root mean square and mean, respectively, of DoD values over stable ground (Anderson, 2019). $a_i$ and $\boldsymbol{\sigma}_{sc}^2$ are the range and sill, respectively, of a spherical semivariogram model with no nugget (Rolstad et al., 2009) fitted to an empirical semivariogram of DoD values over stable ground.

For the calculation of the parameters above, we identified areas of stable ground within the DoDs where true elevation change is zero. We examined orthomosaics and NAIP imagery to manually outline stable ground areas where the land surface had not changed over our 68 year period (e.g., rock outcrops, boulder fields) (Fig. S1). No effort was made to exclude areas of measurement (Section 3.2.3) from the stable ground areas (Anderson and Shean, 2022).

The uncertainty parameters calculated for each DoD are presented in Table 1.

### 3.5. Explanatory terrain characteristics

To examine the terrain characteristics of measured areas on Mount Baker, we generated slope and drainage area rasters from a 2015 lidar Digital Terrain Model (DTM) from WADNR, downsampled to 10-meter resolution. We downsampled to a relatively coarse resolution to remove small-scale roughness features present in the original 1-meter product and calculate slopes representative of hillslope processes. The slope raster was generated using the Horn (1981) algorithm implemented in the xDEM software package (Xdem Contributors, 2021). The drainage area raster was generated using D8 flow direction and flow accumulation algorithms implemented in the Pysheds software package (Bartos et al., 2022), the raster contains a total upslope area value for each pixel. For the subset of pixels within the ten fluvial and hillslope domains, we plotted the distribution of drainage area and slope values. For each erosion polygon, we calculated and plotted the mean slope and maximum drainage area of all pixels. Maximum drainage area represents the magnitude of streamflow that occurs over a given area (Fig. 3).

Nearly 73 % of the study domain have slopes >19°, which is the slope angle identified by Legg et al. (2014) for gully heads on Mt. Rainer, WA, and an approximate low limit for the initiation of saturated landslides in the Cascades Range, WA (Strauch et al., 2018). 32 % have mean slopes >34°, a threshold for fluvial bed failure (Takahashi, 1978; Prancevic et al., 2014).

To explore connections between measured sediment yield and terrain characteristics at the watershed scale, we calculated drainage area, $A$; channel slope, $S_c$; hillslope domain slope, $S_h$; glacial retreat area, $\Delta A_g$; and non-igneous fraction, $F_{ni}$, for each watershed. $A$ is the area of the delineated watershed (Fig. 1). $S_c$ is the slope of the primary stream channel (the fluvial domain), calculated as the difference between the elevation at the watershed outlet point and the elevation where the stream channel meets the maximum glacier terminus, divided by the length of the channel between the two points. $S_h$ is the mean slope raster value in the hillslope domain. $\Delta A_g$ is the change in area of the glacier (Section 3.2.3) between 1977/1979 and 2015, a period of glacier retreat (Fig. 1). Recent studies have identified lithology as a contributing factor to inter-watershed sediment yield variability (Carrivick and Tweed, 2021). As the two most common surface lithologies in our measured bareground areas are andesite flows (igneous) and Pleistocene glacial till and we expect loose surface material to erode more easily than igneous rock, we broadly characterized the surface lithology of each basin with $F_{ni}$, the fraction of bare ground area underlain by a non-igneous surface lithology. $F_{ni}$ characterizes the initial geological conditions unique to each watershed, which exist as a result of the recent volcanic and glacial history of Mount Baker (Section 2). We extracted surface lithologies from a digitized surface geology map (Tabor et al., 2003).

For each of the five explanatory variables, we calculate the coefficient of determination ($R^2$) for both the mean annual sediment yield and mean annual specific sediment yield (SSY) calculated using the 1947–2015 DoD (Section 3.1.4). SSY is calculated by dividing sediment yield by watershed drainage area, $A$.

### 3.6. Watershed sediment yield equations

Relationships developed for long-term channel incision or sediment flux at a channel reach or local grid cell scales are often referred to as geomorphic transport laws (GTLs) and are commonly used in landscape evolution models (e.g., Dietrich et al., 2003). GTLs can relate both local, supply-limited erosion, or global, transport-limited sediment flux to local variables, such as upslope drainage area, local slope, topographic curvature, erodibility, and substrate size (Istanbulluoglu, 2009). Similar empirical relationships have also been used to relate watershed-scale

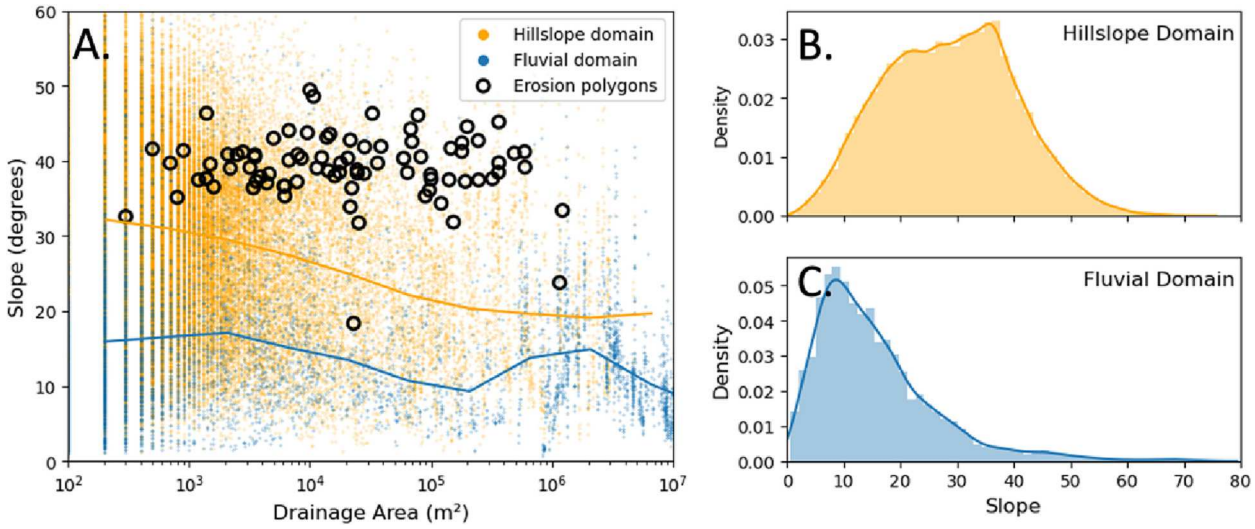


**Fig. 3.** (A) Distribution of slope and drainage area values extracted from a 10 × 10-meter 2015 DTM. Dots show the drainage area and slope values for all pixels in the fluvial domains (blue dots) and all pixels in the hillslope domains (orange dots). Black rings ($n = 85$) show the maximum drainage area value and mean slope value of all pixels within each erosion polygon. Lines show the median slope values for bins of drainage area for all pixels in the fluvial domains (dark blue line) and all pixels in the hillslope domains (red line). (B) Distribution of slope values for all pixels in the hillslope domains. (C) Distribution of slope values for all pixels in the fluvial domain.

erosion to channel slope, relief, and precipitation (Ahnert, 1970; Montgomery and Brandon, 2002; Henck et al., 2011; Portenga and Bierman, 2011).

In this study, we developed nonlinear (power law) empirical equations for watershed-scale sediment yield inspired by GTLs but implemented using spatially averaged topographic and environmental variables (Section 3.5). We considered the relationships between the terrain characteristics $A$, $S_c$, and $S_h$, and the measured absolute sediment yield of ten glacierized basins, and calculated the Nash-Sutcliffe model efficiency coefficient (NSE) of optimized power law models of the form

$$Q_s = kA^m \tag{4}$$

where $Q_s$ is mean annual sediment yield (ton/yr) calculated from the net volumetric change measured in the combined hillslope and fluvial domains and where $A$ may be replaced by $S_c$ or $S_h$. Power law models are not created for the variables $A_g$ and $F_{ni}$ because we do not expect $Q_s$ to approach zero as $A_g$ and $F_{ni}$ approach zero (as we do with $A$, $S_c$, and $S_h$). Our results indicated that $A$ and $S_h$ are positively correlated with $Q_s$, which led us to test a multi-variable power law consistent with the literature,

$$Q_s = kA^m S_h^n, \tag{5}$$

(Dietrich et al., 2013). $k$ is an erodibility parameter and $m$ and n are power law parameters. This model hypothesizes that a basin's sediment yield is controlled by hillslope gradient and flow at the outlet, with drainage area used as a proxy for the latter. We optimized model parameters for our measurements using non-linear least squares regression (scipy.optimize.curve_fit, Virtanen et al., 2020). We excluded watersheds with negative sediment yields (net deposition) from the model fitting process.

### 3.7. Nooksack River sediment budget

To test the hypothesis that glacierized volcanos shed sediments that fill riverbeds downstream, we developed three distinct sediment budgets for the North Fork (NF), Middle Fork (MF), and main stem Nooksack Rivers (combined NF and MF). Four glacierized basins on Mount Baker measured in this study feed into the NF and MF (Fig. 4). The sediment budgets account for our measurements of proglacial basin sediment yield (Section 3.3), DoD-based measurements of stream bank terrace erosion (Scott and Collins, 2021), and measurements of suspended sediment load (Anderson et al., 2019).

Anderson et al. (2019) presented measurements of average suspended sediment load at four gages in the main stem Nooksack River and its three forks (Fig. 4) for water years 2014–2016. Measurements taken at the main stem Nooksack River gage include sediments sourced from the South Fork, which does not have headwaters on Mount Baker (Fig. 4). To address our lack of measurements in the South Fork's headwaters and allow us to compile a sediment budget for the main stem, we subtracted suspended load measurements made at the South Fork gage from those made at the main stem gage. We assumed that the resulting suspended load is the load contributed by the MF and NF. We used a compilation of observed bedload and suspended load rates (Turowski et al., 2010) to estimate a range of total loads expected from the Anderson et al. (2019) suspended load measurements. Scott and Collins (2021) measured volumetric bluff and terrace erosion occurring along the riverbanks of the Nooksack River and its forks (Fig. 4) between 2005 and 2017. We converted these volumetric measurements to mass using the density estimate provided in their study, 2 metric tons/m$^3$. The data from Anderson et al. (2019), Turowski et al. (2010) and Scott and Collins (2021) used in this study are compiled in Table S5.

The upper NF budget includes sediment yield measurements from Mazama basin; it includes no bluff/terrace erosion measurements as there are no such sites upstream of the upper NF gage (Fig. 4). Coleman basin is not included in the upper NF sediment budget because the upper NF stream gage is upstream of where the Coleman basin drainage enters the NF (Fig. 4) (Anderson et al., 2019). The MF budget includes sediment yield measurements from Deming and Thunder basins; no bluff/terrace erosion sites are reported in the MF watershed (Fig. 4). The main stem budget includes sediment yield measurements from Mazama, Coleman, Deming, and Thunder basins and a number of bluff/terrace erosion sites along the main stem and in the North Fork watershed (Fig. 4).

## 4. Results

### 4.1. Intra-watershed measurements

#### 4.1.1. Elevation change maps

In this section we highlight glacier changes and geomorphic processes, in relation to relict LIA landscape features, in two basins, Deming

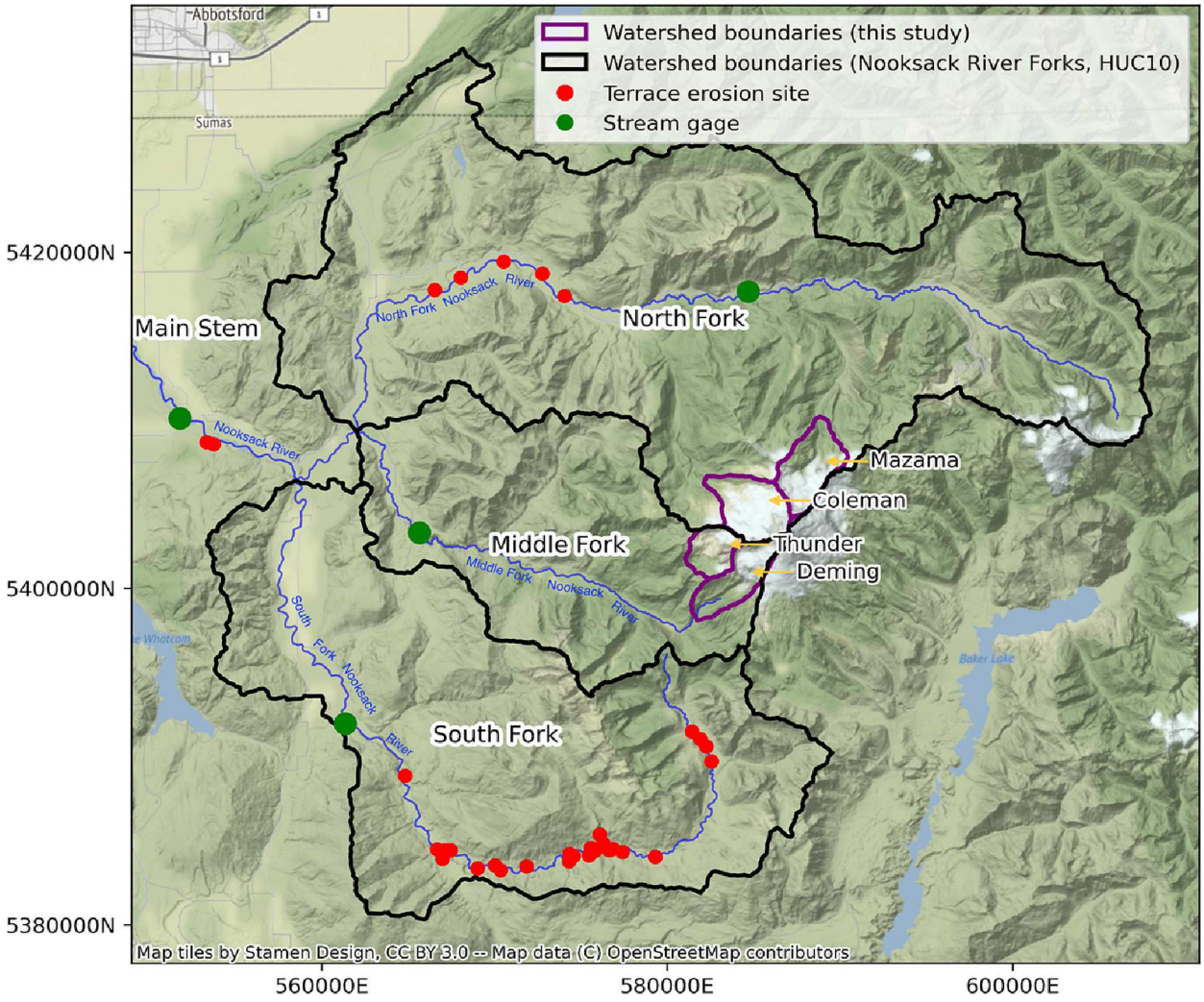


**Fig. 4.** Map of Mount Baker, the three Nooksack River forks and their confluence. Watershed boundaries (this study) are shown in detail in Fig. 1; HUC10 watershed boundaries are from the NHDPlus database. Terrace erosion sites are those measured in Scott and Collins (2021). Stream gages shown are the gages used in our Nooksack River sediment budget, measured in Anderson et al. (2019).

and Rainbow. Results for the other two high erosion basins are included in the Supplementary Materials (Figs. S5 and S6).

In the Rainbow proglacial basin, we observe glacier advance between 1947 and 1977 and retreat beginning sometime thereafter, consistent with the literature (Dick, 2013). Most geomorphic change occurred along the LIA lateral moraines. A number of gullies incised into the southern (north facing) LIA moraine beneath fluctuating glaciers and incision occurred, in some gullies, during multiple, discrete measurement periods (Fig. 5A and C). A large landslide occurred on the southern moraine between 1947 and 1970 (Transect 1 in Fig. 5A, B) and its deposit is visible on the valley floor (Fig. 5A I). On the northern (south facing) moraine, a rotational slump, which has been active since before 1947 (Fuller, 1980), moved during all periods of measurement and protrudes into the valley floor (Fig. 5A II). Some scour of the stream channel is visible downstream of the landslide deposit and upstream of the LIA glacial maximum boundary (Fig. 5A III). Apart from the landslide deposit (Fig. 5A I), we observed minimal depositional signals apart from two small debris cones downslope of eroded gullies (Fig. 5A V and VI). Within the 19th century debris flow deposit, small elevation changes appear associated with redistribution of sediments by the stream channel (Fig. 5A IV).

In the Deming proglacial basin, we observe similar glacier behavior and a similar distribution of erosion signals, with most erosion occurring near the crest of the LIA moraines. Compared to Rainbow basin, more erosion occurred along the margins of the fluctuating glacier. Towards the downstream end of the valley, the LIA moraine laterally retreated >20 m and became steeper between 1947 and 2015 (Transect 2 in Fig. 6A and C). Gully erosion (Fig. 6 I), land sliding (Fig. 6A, the June 6, 2013 debris flow source area), and stream channel scour (Transect 1 in Fig. 6A and B) are evident in Deming basin. We identified source areas associated with May 31 and June 6, 2013, debris flow events (Tucker et al., 2014) and measured, using erosion polygons (Fig. 6A), −70,000 $m^3$ and − 92,000 $m^3$ of volumetric change for these events, respectively. These measurements are consistent with the Tucker et al. (2014) estimate of 100,000 $m^3$ for the May 31 event. In the stream channel, incision or scour occurs both close to the fluctuating glacier boundary (Transect 1 in Fig. 6A and B) and approximately 1.5 km downstream, within the 1927 debris flow deposit (Fig. 6A II). We observed limited deposition in Deming basin; some positive elevation change occurred in the stream channel and at the foot of the eroding moraine (Transect 2 in Fig. 6A and C).

In the other two high-erosion watersheds (Coleman and Mazama), we observed similar erosion patterns, with most erosion occurring on steep LIA moraine sidewalls (Figs. S5 and S6). These measurements also demonstrated limited deposition and minor changes to the primary stream channels during the 68-year period.

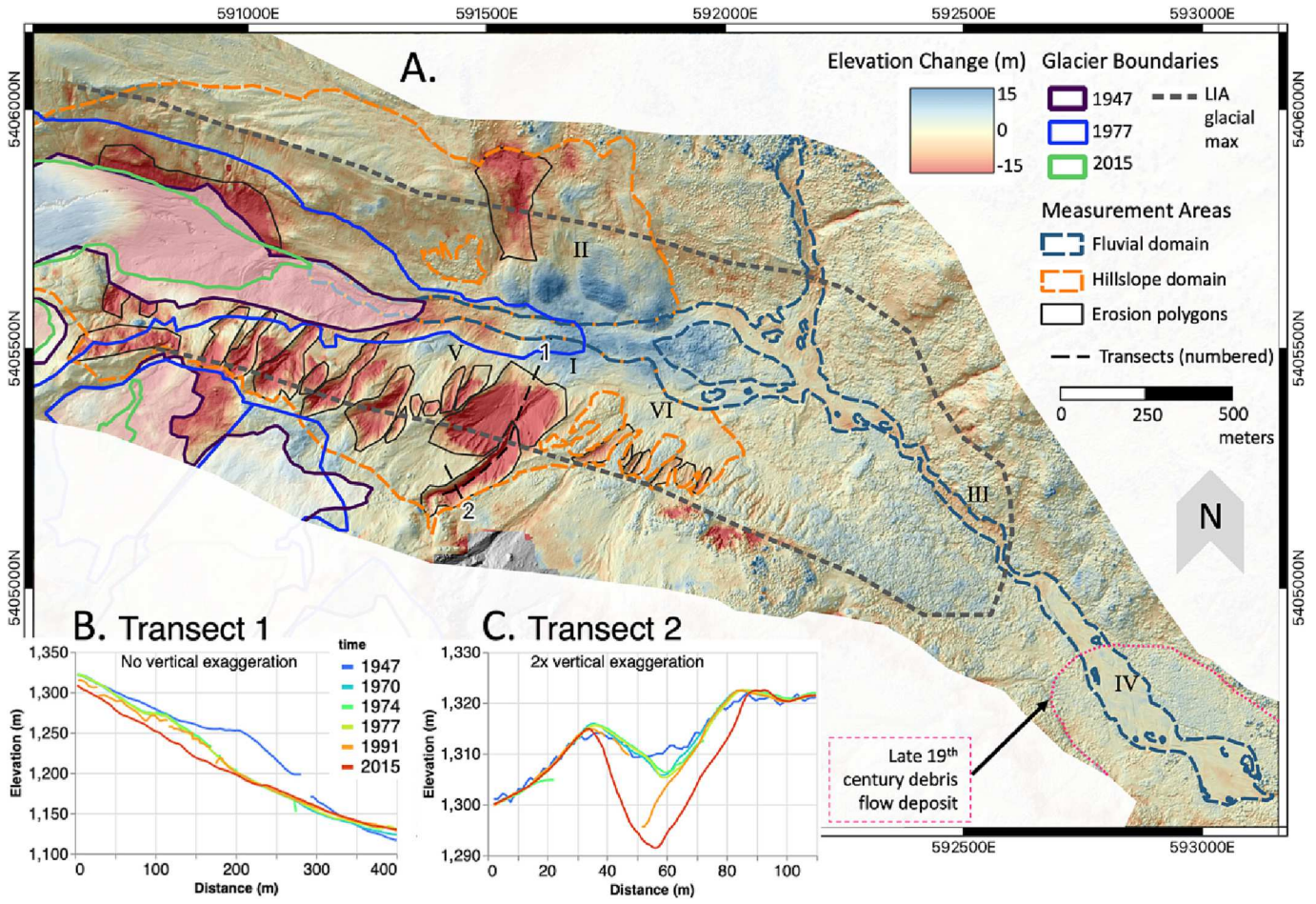


**Fig. 5.** (A) Rainbow Glacial valley 68-year elevation change DoD (2015 minus 1947) overlaid on the 2015 lidar DEM hill shade. Elevation change color ramp is saturated at −15 and +15 m to bring out detail, though many signals are larger. Opaque polygons cover elevation changes related to changing glacial extent. The 1977 glacier boundary shows the near-maximum extent of Rainbow Glacier during our study period. Roman numerals (black text) indicate features discussed in the text. The pink, dashed outline indicates the extent of a late 19th century debris flow deposit inferred from lidar topography (Fuller, 1980; Hyde and Crandell, 1978). Coordinates are in projected coordinate system Universal Transverse Mercator zone 10 N. Cross-sectional profiles for Transects 1 and 2 for different years are shown in panels (B) and (C).

#### 4.1.2. *Volumetric change time series*

To explore how geomorphic change rates vary in time and to characterize the sediment connectivity of proglacial basins, we measured change on hillslopes and in stream channels using our DEM time series (Fig. 2). We present time series of gross erosion, gross deposition, and cumulative net volumetric change in four basins alongside a climate index time series adapted from the literature (Fig. 7) (Anderson and Konrad, 2019).

In all four high erosion basins, change measured prior to 1970 contributed the majority of cumulative net volumetric change (Fig. 7I–L) and gross hillslope and fluvial erosion were generally greatest during the same period (Fig. 7A–H). Hillslope erosion rates were generally lower between 1970 and 1990 in all valleys; hillslope erosion rates in Deming and Mazama basins increased after 1990 (Fig. 7E–H). Fluvial erosion rates were elevated before 1970 and after 1990 in Coleman, Deming, and Rainbow basins (Fig. 7A–D). Rates of volumetric change in the hillslope domains were generally an order of magnitude larger than in the fluvial domains and hillslope erosion signals were generally larger than hillslope deposition signals (Fig. 7A–H).

Variations in erosion rates can be related to climate. The annual Pacific decadal oscillation (PDO) index, an index based on temperature and precipitation anomalies, demonstrates colder-wetter periods between approximately 1940–1970 and the late 1990s–2015, and a hotter-drier climate otherwise (Fig. 7M) (Anderson and Konrad, 2019). Colder-wetter periods approximately align with increased hillslope and fluvial gross erosion rates in Deming, Mazama, and Rainbow basins (Fig. 7B–D, F–H) and increased cumulative net volumetric change in all basins (Fig. 7I–L).

### 4.2. *Inter-watershed measurements*

In this section, we compare the absolute and normalized annual sediment yields and terrain characteristics of ten proglacial basins (Table S6) and show geomorphic transport equations fitted to our data. Absolute annual sediment yields vary widely across Mount Baker with a maximum yield of 89 ± 8.6 kt/year in Deming basin and yields in Boulder and Thunder basins indistinguishable from zero (Fig. 8A).

SSYs were more consistent across the ten basins, Easton basin yielded 4.7 kt/km$^2$/yr and Deming basin 7.6 kt/km$^2$/yr, the average of non-negative SSY measurements is 4.6 kt/km$^2$/yr (Fig. 8B, Table S6). Our measurements in units of meters per year indicate denudation rates of approximately 3 mm/yr in the six basins with yields distinguishable from zero. Two basins, Squak and Talum, experienced net deposition, up to 21 ± 11 kt/year. We interpret negative sediment yield measurements as indication that moraine formation and/or other glaciogenic sediment deposition exceeded erosion. It is also possible that material from outside our measurement areas but within the watershed was transported into the measurement area or that vegetation growth that could

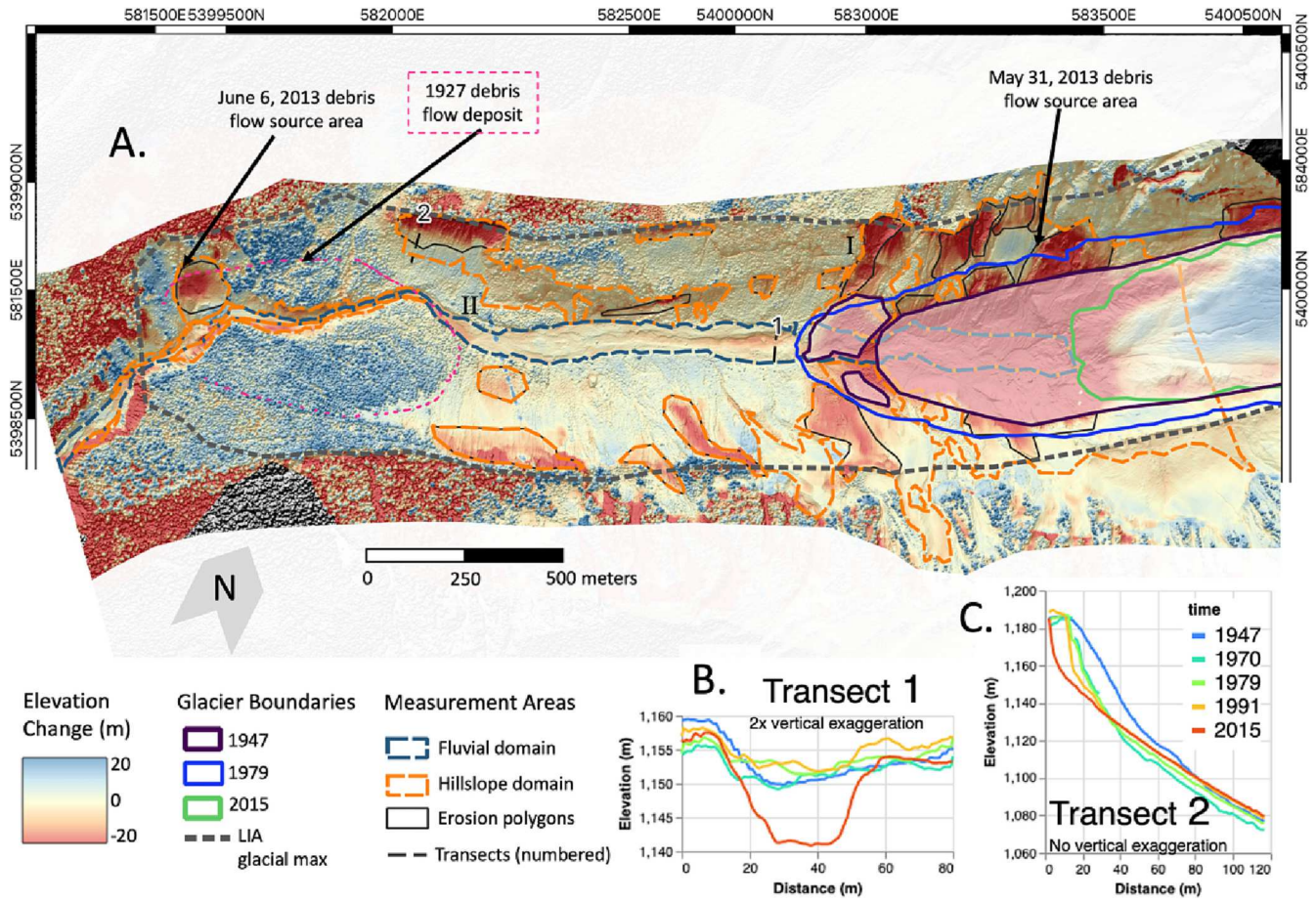


**Fig. 6.** (A) Deming Glacial valley 68-year elevation change DoD (2015 minus 1947) overlaid on the 2015 lidar DEM hill shade. Elevation change color ramp is saturated at −20 and +20 m to bring out detail, though many signals are larger. Opaque polygons cover elevation changes related to changing glacial extent. The 1979 glacier boundary shows the near-maximum extent of Deming Glacier during our study period. Roman numerals (black text) indicate features discussed in the text. Coordinates are in projected coordinate system Universal Transverse Mercator zone 10 N. Cross-sectional profiles for Transects 1 and 2 are shown in panels (B) and (C).

not be excluded from measurement contributed positive elevation change signals.

Fig. 9 shows the relationships between measured absolute and SSY rates and explanatory variables for topographic characteristics, glacial retreat, and lithology.

Absolute sediment yield is positively correlated with drainage area, hillslope domain slope, and nonigneous fraction ($R^2$ of 0.82, 0.52, and 0.54, respectively) and negatively correlated with channel slope ($R^2$ of 0.67). Glacial retreat area (area of land surface exposed by glacial retreat between 1977/79–2015) does not predict sediment yield well. Drainage area predicts absolute sediment yield better than SSY ($R^2$ of 0.82 vs 0.44, Fig. 9A and F). Nonigneous fraction predicts SSY better than absolute sediment yield ($R^2$ of 0.82 vs 0.54, Fig. 9J and E). Channel slope and hillslope domain slope predict absolute and SSY with similar skill (Fig. 9B, C, G, H). Although Squak and Talum basins were not included in the model fitting process, the two net depositional basins continue most of the linear trends exhibited by the other eight basins. The two net depositional basins have the smallest drainage area of all study basins (Fig. 9B), the steepest channel slopes (Fig. 9C), relatively low hillslope domain slopes (Fig. 9D) and the greatest proportions of underlying igneous lithology (Fig. 9F).

The distribution of nonigneous fraction measurements indicate that the ten basins can be categorized into two groups, those underlain by >68 % igneous rocks ($F_{ni} < 0.32$), which are Holocene-Pleistocene and Quaternary andesite flows and Cretaceous gabbro; and those underlain by <30 % igneous rocks ($F_{ni} > 0.7$), with Cretacious-Jurassic marine sedimentary rocks, Holocene-Pleistocene talus deposits, and Pleistocene glacial till and drift the primary surface lithologies (Fig. 9F, S3, S4, Table S6) (Tabor et al., 2003). The four basins with igneous-dominant lithologies all have either negative sediment yields or sediment yields indistinguishable from zero within uncertainty (Fig. 9F). To examine climate-related drivers to a first order, we compared 800-meter gridded average annual precipitation (1981–2010) reanalysis data (PRISM Climate Group, 2014) across basins and found that precipitation rates did not correlate with sediment yields. We did not examine additional climate-drivers.

The power law model incorporating both drainage area and hillslope domain slope (Eq. (5)) predicts observed sediment yield well (NSE = 0.86, Fig. 10), but only slightly improves upon the predictive power of drainage area alone (NSE = 0.82, Fig. 9A). Including other variables in multivariate power laws did not offer further improvement.

### 4.3. Nooksack River sediment budget

Mean annual sediment budgets for the upper NF, MF, and main stem Nooksack Rivers are presented in Table 2.

Considering the full range of estimated total loads, proglacial sediments measured in our study may account for as little as 11 % (upper NF gage) or as much as 59 % (MF gage) of total load estimated from in-situ riverine measurements (Table 2). The main stem sediment budget provides a more complete comparison as it includes measurements from a number of NF terrace and bluff erosion sites upstream of the main stem

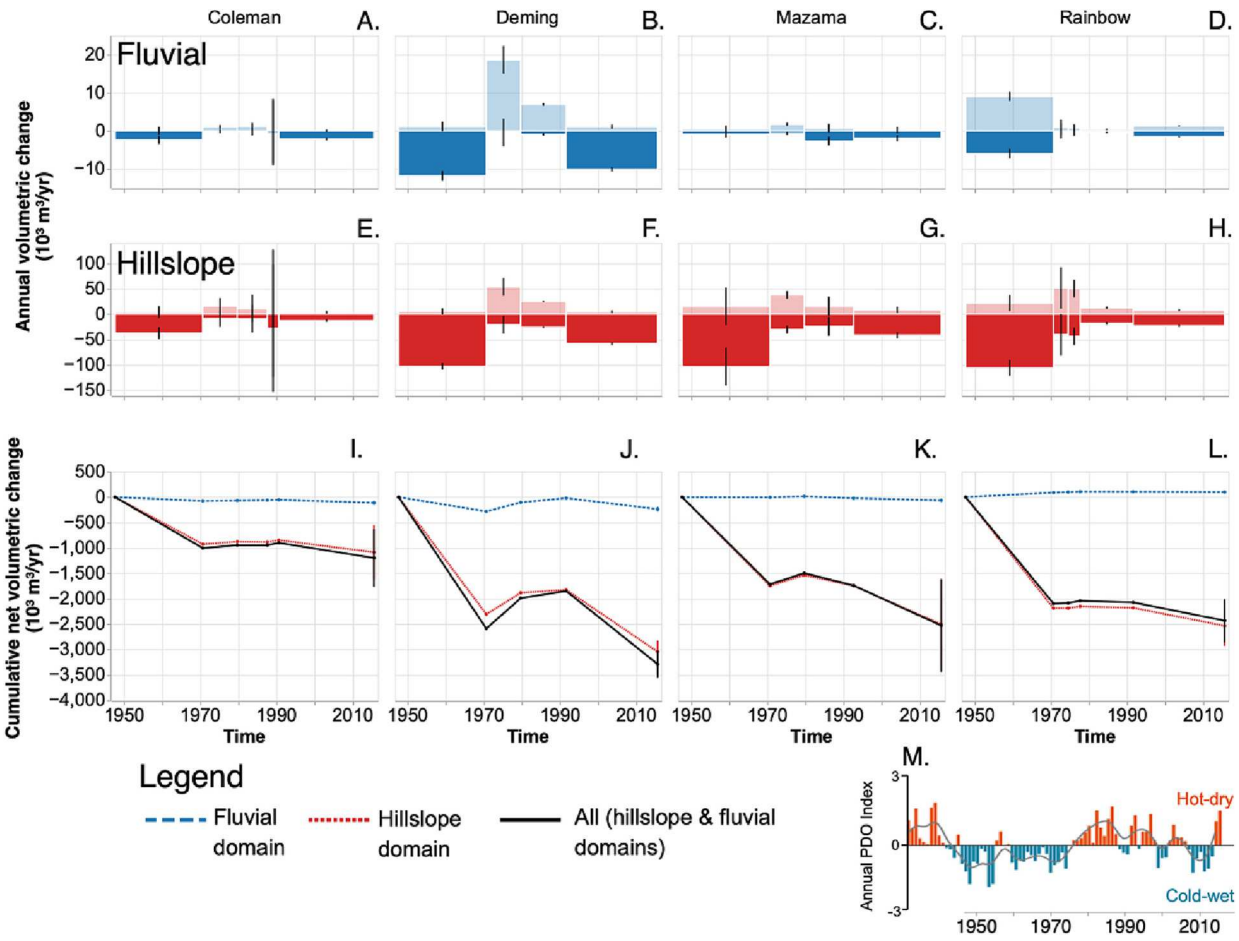


**Fig. 7.** Gross volumetric change measured in fluvial (A–D) and hillslope (E–H) domains for the four high erosion sites; gross erosion is negative and shown in opaque colors, deposition is positive and shown in semi-transparent colors. (I–L) Cumulative net volumetric change in the four high erosion sites in the fluvial and hillslope domains. "All" shows the cumulative change in the combined fluvial and hillslope domains. (M) Mean annual Pacific decadal oscillation (PDO) index, adapted from Anderson and Konrad (2019).

gage but downstream of the upper NF gage (Fig. 4). Our main stem sediment budget indicates that proglacial erosion may account for 18–32 % and bluff and terrace erosion 8–13 % of riverine total load (Table 2).

## 5. Discussion

Our intra-watershed observations are used to infer sediment connectivity, dominant sources of erosion, and the efficiency with which watersheds deliver sediments downstream in relation to climate variability.

### 5.1. Intra-watershed spatial variability

Within the four high erosion basins on Mt. Baker, we observed that most erosion occurred on LIA moraines and that gully headward erosion allows sediment transport across moraine crests, which may otherwise disrupt sediment connectivity (e.g., Transect 2 in Figs. 5A, 6A I) (Mancini and Lane, 2020). In Deming basin, we observed some steepening of moraines over time (Fig. 6C), similar to the study site of Curry et al. (2009) where the dip of mica-schist clasts allows high-angle slope stability. Local lithology, in part controlled by glacial deposition, may create variation in how erosion processes proceed.

We found that while erosion occurred throughout the proglacial zone, it is concentrated near recently retreated glacier boundaries. In Rainbow basin, large erosion signals exist no further downstream than the 1977 glacier boundary (Fig. 5A) and in Deming basin, a higher density of erosion signals surrounds the fluctuating glacier boundaries (Fig. 6A). In a similar stratovolcano site (Mount Rainer, WA), Legg et al. (2014) predict that debris-flow frequency will increase with continued glacial retreat due to positive slope-elevation relationships on glacierized stratovolcanoes (i.e., glacial retreat exposes more steep slopes). In Deming and Rainbow basins, recent deglaciation does not appear to have exposed steeper parts of the landscape and nearly all measured erosion sites are well above a debris-flow initiation threshold slope of 34° (Fig. 3A) (Takahashi, 1978; Prancevic et al., 2014). Deglaciation appears to have still initiated mass failure and debris flow, perhaps via debuttressing of over-steepened landforms, as is suspected for the source area of the May 31, 2013, debris flow (Fig. 6A) (e.g., Cody et al., 2020).

One notable result of our intra-watershed measurements is the apparent effectiveness, over decadal timescales, with which proglacial basins export sediment. Of the 18 measurements of net volumetric change made in four basins, 11 had net erosion (Fig. 7). Nine of those measurements had RSI values >0.5 (Fig. 11, Eq. (2)).

The mean RSI of the 11 net erosion measurements is 0.73 and the median 0.79. These high RSI values indicate that most sediment movement within the four high erosion catchments lead to a net export.

### 5.2. Intra-watershed temporal variability

While we expect decadal climate fluctuations (Fig. 7M) to influence erosion rates by modifying rainfall patterns and the resulting shear stresses exerted on the land surface, identifying these influences in our measurements is challenging due to the coarse temporal resolution of

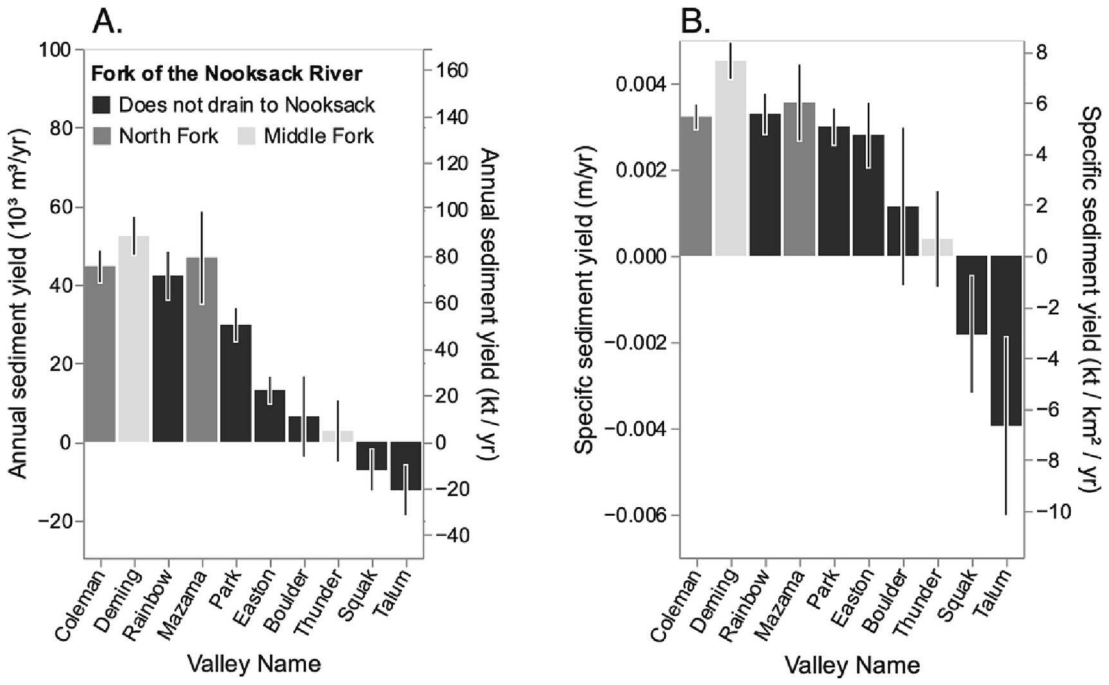


**Fig. 8.** Annualized sediment yield between 1947 and 2015 in all measured proglacial watersheds. Sediment yields in kilotons per year are calculated by converting volumetric change measurements using a porosity of 0.35 and rock density of 2600 kg/m$^3$ (Section 3.3). Watersheds with negative yield values are net depositional.

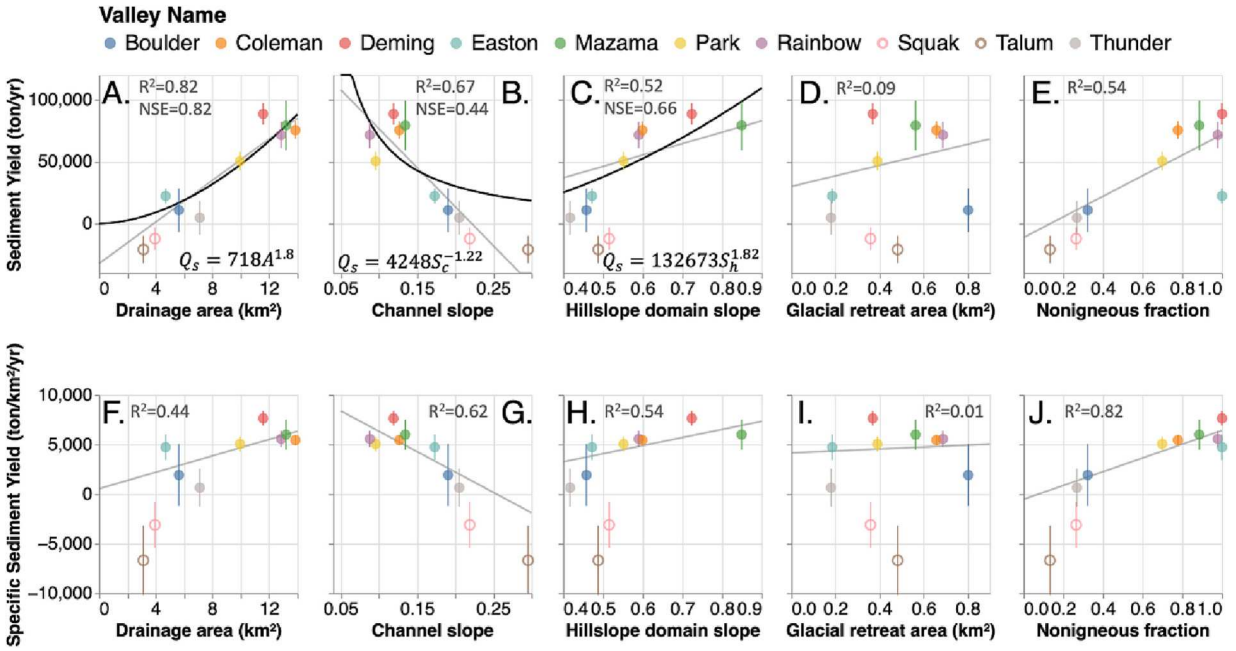


**Fig. 9.** Relationships between terrain characteristics and mean annual sediment yields (Panels A–E) or mean annual specific sediment yields (Panels F–J) calculated for the 1947–2015 period in basins on Mount Baker (Fig. 8). Uncertainty for each sediment yield measurement (Table S6) is represented by vertical bars. Lines show the linear (light grey) and power (dark grey) model fits. Open circles represent net depositional valleys, which are not included in the model fits. Three fitted power law equations are shown in Panels A–C. Nash-Sutcliffe model efficiency (NSE) values are reported for fitted power law models, $R^2$ values are reported for all relationships.

our DEM dataset (Fig. 2). Even so, our measurements suggest a link between climate and proglacial erosion rates. The 1947–2015 period lasts one full oscillation of the PDO and high erosion rates prior to 1970 and after 1990 align with climatologically cold-wet periods (Fig. 7). The highest RSI values were measured prior to 1970 and after 1990, and all net depositional (RSI < 0) measurement periods overlap the 1975–2000 period of hot-dry climate, indicating that erosion and sediment export rates increase with colder, wetter weather (Fig. 11). These observations are consistent with other studies of glacierized stratovolcano erosion in the same region. Sediment core measurements in Alder Lake, which traps sediment delivered from Mount Rainier, indicate elevated sediment delivery rates between 1945 and 1955, lower rates 1955–1985, and increased rates thereafter (Czuba et al., 2012). All of these findings suggest periodicity in sediment export, with periods of sediment

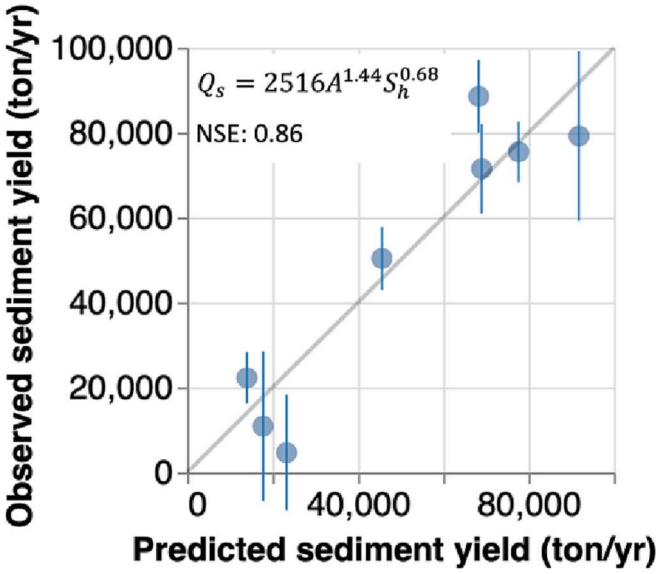


**Fig. 10.** Measured sediment yield versus the predicted sediment yield for the area and hillside slope model (Eq. (5)). The fitted power-law equation is shown in the figure.

accumulation during hot-dry climate and transport during cold-wet climate. During the hot-dry period, hillslope erosion by mass wasting and gully erosion continued at a reduced rate, while fluvial transport (gross fluvial erosion) was reduced almost entirely (Fig. 7).

In addition to climate variations, the relatively high erosion rates between 1947 and 1970 and 1990–2015 may be partly attributable to preceding glacier retreat. Deglaciation between 1930 and 1945 exposed up to 1 $km^2$ (Dick, 2013) and between 1979 and 2015 up to 0.8 $km^2$ of land surface in individual valleys (this study; Table S1). In some cases, we are confident that glacier retreat instigated erosion (the May 31, 2013, debris flow, Section 5.1). However, we also observed that some areas that lost ice cover before 1947 eroded throughout our measurement period (e.g., the June 6, 2013, debris flow source area in Fig. 6a, gullies on the moraine south of Rainbow glacier in Fig. 5A). These observations together suggest that changes in sediment yield are linked to climate oscillations through two pathways–via climate's effect on glacier advance/retreat and via climate's effect on precipitation patterns.

Our 68-year record of landscape change begins approximately a century after the end of the LIA (Harper, 1993; Dick, 2013), when erosion rates should be relatively high and decay thereafter, as unstable landforms are broken down (Carrivick and Heckmann, 2017). However, as the model of Antoniazza and Lane (2021) suggests, sediment output from deglaciating systems can follow a more complex pattern, involving relict effects of multiple readvance and retreat periods. For net sediment exporting basins, erosion rates we calculated are in the 0.2–4 mm/y range with an average of ~3 mm/yr. The long-term average erosion rates of the Cascade Mountains, where Mount Baker is located, range between 0.02 and 0.5 mm/y over roughly the last several million years

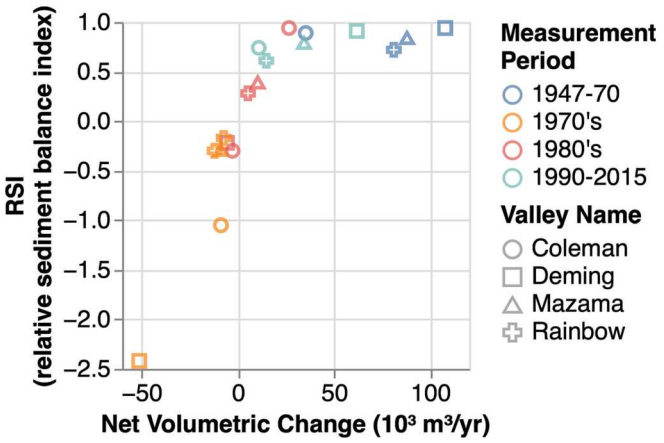


**Fig. 11.** Relative sediment balance index (RSI) and net volumetric change calculated for each measurement in the four high erosion valleys (Fig. 7). RSI is the ratio of net volumetric change to gross erosion (including measurements in both the hillslope and fluvial domains) (Eq. (2)). The measurement period corresponds to the time periods shown in Fig. 7; 1990–2015 includes the measurements beginning in 1991 (Rainbow and Deming) and 1992 (Mazama).

**Table 2**
Sediment budget for the upper North Fork, Middle Fork, and main stem Nooksack Rivers including our measurements of proglacial basin sediment yield (Section 3.3), DoD-based measurements of stream bank terrace erosion (Scott and Collins, 2021), and measurements of suspended sediment load (Anderson et al., 2019). Suspended sediment load measurements in each fork are used to infer a range of total load measurements using the results of Turowski et al. (2010). We calculate the percentage of the estimated total load flux that can be attributed to proglacial erosion using measurements from this study, and bluff/terrace erosion using reanalysis of measurements from Scott and Collins. We calculate specific sediment yields for both the suspended and total loads by dividing estimates of suspended and total load by the watershed areas presented in the table. Original measurements from Anderson et al., Turowski et al., and Scott and Collins (2021) are provided in Table S5.

| Measurement type: | Riverine suspended sediment load | Riverine total load | Bluff/terrace erosion | | Proglacial erosion | |
|---|---|---|---|---|---|---|
| Source: | Anderson et al., 2019 | Anderson et al., 2019 & Turowski et al., 2010 | Scott and Collins, 2021 | | This study | |
| Measurement time period: | 2014–2016[1] | | 2005–2017[2] | | 1990–2015; 1947–2015[3] | |
| Units: | Kilotons/year (kilotons/$km^2$/year) | | Kilotons/year | Percent of total load[4] | Kilotons/year | Percent of total load[4] |
| Upper North Fork Nooksack (272 $km^2$) | 240 (0.882) | 250–530 (0.92–1.9) | 0 | 0 | 58 | 17 % (11–23 %) |
| Middle Fork Nooksack (192 $km^2$) | 170 (0.885) | 180–430 (0.94–2.2) | 0 | 0 | 106 | 41 % (25–59 %) |
| Main stem (combined North and Middle Forks)[5] (1191 $km^2$) | 540 (0.453) | 570–980 (0.48–0.82) | 74 | 10 % (8–13 %) | 180 | 26 % (18–32 %) |

1. Anderson et al. (2019) presents averaged suspended sediment load measurements for the water years 2014–2016.
2. Bluff measurements are taken from three lidar DEMs of Difference (DoD) with date ranges 2005–2015, 2005–2017, and 2006–2017.
3. Rates for each fork are computed using the most recent DoD time interval for each basin. North Fork (Mazama basin) is 1992–2015, Middle Fork (Deming and Thunder basins) combines measurements 1991–2015 for Deming and 1947–2015 for Thunder.
4. Ranges presented represent calculations using the range of total loads inferred from Turowski et al. (2010). Single values represent the average of the range.
5. Main Stem (combined North and Middle fork) suspended load estimates are calculated from Anderson et al. (2019), using the main stem measurements minus contributions from the South Fork. Main stem drainage area excludes the drainage area of the South Fork.

(Reiners et al., 2002, 2003). On average, about four times higher erosion rates were found over the last millennia (0.08–0.57 mm/y) in the Cascades, in positive correlation with precipitation and elevation, but excluding any volcanic topography (Moon et al., 2011). These higher rates in the last millennia are consistent with findings in the Late Holocene and the LIA glacier advance periods (2.5 k BP–1850) in most deglaciating rivers (e.g., Elverhøi et al., 1998; Hasholt et al., 2000; Koppes and Hallet, 2006; Antoniazza and Lane, 2021). Erosion rates in volcanically disturbed rivers also far exceed erosion rates of surrounding rivers, in particular following eruptions, for similar drainage area scales as our study basins (Koppes and Montgomery, 2009). Based on this evidence, the decadal erosion rates we found are on par with other similar proglacial basins, and do not show any strong indication of paraglacial decline (Antoniazza and Lane, 2021). Given future accelerated glacier retreat (Frans et al., 2018) and existing steep relict topography (Fig. 3) we anticipate that high erosion rates will likely sustain in the region with anthropogenic climate change.

### 5.3. Inter-watershed erosion rates

#### 5.3.1. Specific sediment yields

Excluding net depositional basins, our measurements of SSY, which range from 650 to 7600 and average 4600 ton/km$^2$/yr (Fig. 8), are consistent with decadal measurements from Alaska (4000 ton/km$^2$/yr), the European Alps (100–7000 ton/km$^2$/yr), and the Himalayas (100–10,000 ton/km$^2$/yr) (Carrivick and Tweed, 2021).

Our measurements demonstrate a decrease in SSY with increasing basin size (between 10 and 1000 km$^2$) (e.g., Hinderer et al., 2013). We estimated 4600 ton/km$^2$/yr in glacierized headwater basins (average area 10 km$^2$, Fig. 8), ~920–2200 ton/km$^2$/yr in river valleys downstream (basin area ~200 km$^2$, upper NF and MF gages, Fig. 4); and ~500–800 ton/km$^2$/yr in the main stem Nooksack River, downstream of where the NF and MF join and enter lowland plains (basin area 1000 km$^2$, main stem gage Fig. 4, Table 2).

In the upper Nisqually River (590 km$^2$), which drains Mount Rainier, estimated total SSY from bathymetric surveys was 1209 ton/km$^2$/yr and estimates for an adjacent forested catchment were 77 ton/km$^2$/yr (Czuba et al., 2012; Anderson et al., 2019). Czuba et al. concluded that the SSY of basins draining glacierized stratovolcanos can be an order of magnitude larger than that of basins draining forested uplands. Our measurements agree in that the SSYs of the Nooksack River's glacierized, stratovolcano headwaters exceed the SSY measurements in the same system downstream, measurements that incorporate contributions by both glacierized and forested headwaters.

Compilations of regional SSY data from glacierized and glaciated (formerly ice- or glacier-covered) basins in British Columbia show a decrease in SSY with drainage area in basins <10 km$^2$ and > 30,000 km$^2$, and increase for basins at intermediate sizes (Slaymaker, 2018). Weak negative SSY-drainage dependence was reported from European Alps (Hinderer et al., 2013) and Norway (Bogen, 1996) and no apparent relation was identified in a compilation of a global dataset (Carrivick and Tweed, 2021). A negative trend in our data provides evidence to elevated erosion rates in upland proglacial areas, generally consistent with the model of Slaymaker (2018), albeit with decreasing SSYs over a different drainage area range than reported in the literature (see Fig. 9 and 13 in Slaymaker, 2018).

The aforementioned studies that explore SSY-drainage area relations used data with varying temporal resolution from different basins and regions, spanning different climates, lithologies, and valley morphologies (sediment stores) to find relationships between SSY and drainage area. Our measurements provide a unique study of nested basins, and address a dearth of SSY estimates in North America (Carrivick and Tweed, 2021), but they do have some limitations. Our reconstruction of SSYs in the NF and MF of the Nooksack (Fig. 4, Table 2) are only based on two years of data and the differences between SSY values at proglacial watersheds and the downstream gages may be within the natural variability of inter-annual sediment loads. Additionally, our DEM-based SSY measurements in proglacial basins assume that net volumetric change within a basin is directly related to net export from that basin. The presence of vegetation in some depositional areas in our study sites (e.g., downslope of Transect 2 in Fig. 6A) limits our ability to measure deposition such that we may overestimate sediment yields. Conversely, the limited extent of our DEM timeseries and measurements (Figs. 1, 2), along with our inability to account for subglacial sediment sources, may lead to underestimation. In two watersheds, our DEM-based sediment yield measurements are negative, which is either the result of extensive glaciogenic sedimentation or our imperfect measurement methodology (Section 4.2). Further data are needed for more conclusive findings. We call for more systematic nested watershed analysis in river basins using a combination of modern and traditional measurement methods.

#### 5.3.2. Lithology and terrain characteristics

In addition to allowing for comparison with global estimates, our measurements of proglacial sediment yield allow us to examine what factors control variability across ten watersheds on Mount Baker. The primary control appears to be lithology. Two of the three low-yielding basins (Boulder and Thunder) as well as the two net depositional basins (Squak and Talum) are underlain primarily by (igneous) andesite flows and non-igneous fraction is the strongest predictor of SSY ($R^2$ of 0.82, Fig. 9J, S4). Drainage area also seems to be a primary control, at least on non-normalized sediment yield ($R^2$ of 0.82, Fig. 9A). We examined relationships between predictive variables (Fig. 9) and found that nonigneous fraction positively predicts drainage area and hillslope domain slope and negatively predicts channel slope (Fig. 12).

Qualitatively, we observed that high-yielding basins (Coleman, Deming, Mazama, Rainbow, Park) have relatively narrow, confined proglacial zones with steep valley walls and long glacial “tongues” that feed into U-shaped valleys with low-gradient valley floors. These basins are spread around Mount Baker from the southwest side (Deming) clockwise to the northwest side (Rainbow and Park). Low-yielding basins (Talum, Squak, Easton, Thunder) have less confined proglacial zones with more planar topography, steeper channels (Fig. 9B and H), and are mostly on the southeast side of Mount Baker (Fig. 1). The ability of surface lithology to predict sediment yield (Fig. 9) and topographic characteristics (Fig. 12) and the distinct topographies of high and low yielding basins (U-shaped vs broad-planar) together suggest that lithology and valley topography are linked through Mount Baker's Pleistocene to Holocene glacial and volcanic history (Section 2). Surface lithology may predict sediment yield well only in part because of how erodibility varies with lithology (Section 3.5). These interrelated factors may be difficult to incorporate into future modeling efforts. Notably, Easton is an outlier in the sediment yield - nonigneous fraction relationship (Fig. 9E) but not when sediment yield is normalized (Fig. 9J), emphasizing the importance of examining normalized sediment yields as the result of land surface characteristics.

Despite strong lithological controls, including non-igneous fraction in multivariate power law models did not offer improved predictive ability. Our model incorporating drainage area and hillslope domain, $Q_s = 2516A^{1.44}S_h^{0.68}$ (NSE = 0.86, $n = 8$; Fig. 10), showed the most promise. This model implies that flow of water over the landscape, using drainage area as proxy for streamflow, and hillslope gradient are the dominant controls on a granular transport process, which we broadly consider as debris flow (Istanbulluoglu et al., 2003; Legg et al., 2014). While the various equations we tested facilitate our understanding of the erosive behavior of proglacial watersheds, these simple formulations are based on a small sample size (n = 8) and as such are not yet capable of modeling future changes in glacierized landscapes.

### 5.4. Evidence for debris flows as a primary process

While geomorphic transport laws generally rely on channel slope (not hillslope gradient) as proxies for critical shear stress and stream

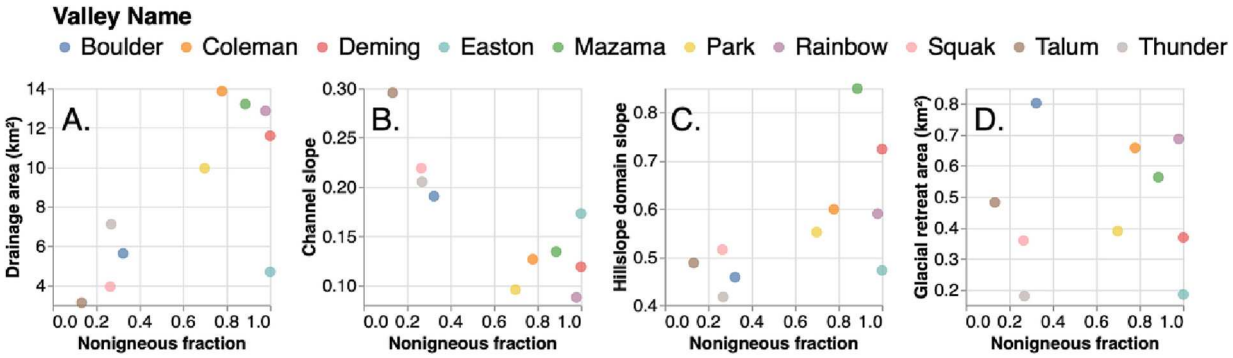


**Fig. 12.** Variable interactions between terrain characteristics for ten basins on Mount Baker.

power, we found a negative correlation between sediment yield and channel slope ($R^2 = 0.67$, Fig. 9B) and positive correlation between yield and hillslope slope ($R^2 = 0.52$, Fig. 9C). We interpret this as indication that debris flows sourced from hillslopes are the primary erosion mechanism and low-angle stream channels in high-yielding basins do not limit export of material. High RSI values (Fig. 11, Section 5.1) and gross erosion measurements that greatly exceed gross hillslope and stream channel deposition measurements (Fig. 7) also support this hypothesis, as debris flows probably have momentum to effectively deliver sediment past the watershed outlet and leave few depositional signals (Section 5.1). While we do observe some deposition on hillslopes (e.g., debris cones shown in Fig. 5A V and VI), depositional landforms appear few and far between.

Our estimate of 162,000 $m^3$ of erosion for the two confirmed 2013 debris flow events in Deming basin (Section 4.1.1) accounts for approximately 12 % of the gross hillslope erosion measured during the 1991–2015 period (57,880 ± 2750 $m^3$/yr, Fig. 7 & Table S2). Tucker et al. (2014) observed that deposits from the 2013 events partially eroded within weeks. We observed that the source area of the May 31 event is adjacent to and across the valley from similarly sized erosion scars (Fig. 6A).

These observations suggest that debris flows account for a substantial portion of sediment exported from proglacial basins and are the primary erosion process in the proglacial zones of Mount Baker. While debris flow events measured using data in this study are small relative to some events on Mount Baker recorded in the literature, such as the 10 million $m^3$ 1927 debris flow (Section 2, Table S7), evidence of larger debris flows further corroborates our conclusions.

### 5.5. *The role of proglacial sediments at the river basin scale*

Our sediment budgets suggest that proglacial sediments make up a notable portion of riverine sediments in the Nooksack River, ranging from 11 to 59 % of total load in the upper NF and MF and 18–32 % in the main stem Nooksack River (Table 2). Contributions by proglacial basins exceed contributions by stream terrace and bluff erosion in the main stem, with 8–13 % of riverine sediments accounted for by terrace and bluff erosion (Table 2). Assuming the upper estimates of the two sediment sources in our budget, terrace/bluff and proglacial erosion contribute a combined 45 % of annualized sediment load in the main stem Nooksack River (Table 2), leaving 55 % of riverine sediment unaccounted for. Our estimate of proglacial sediment contributions in the main stem, 180,000 tons/yr (Table 2) accounts for a notable 18 % of the total load rate measured in the Nooksack River near its outlet at Bellingham Bay, 990,000 tons/yr (Ferndale gage, Anderson et al., 2019). The four proglacial basins have a combined area of 46 $km^2$ (Table S6) and the gage near Bellingham Bay an upstream area of 2036 $km^2$. Our sediment budgets lend support to the notion that proglacial sediments are important for the entire Nooksack River system and that variations in proglacial sediment yield are likely to modify aggradation rates downstream (Anderson and Konrad, 2019).

## 6. Conclusions

In ten watersheds on a glacierized stratovolcano in western Washington, we measured erosion processes, their contributions to sediment yields, and how erosion rates varied in space and time between 1947 and 2015.

- Most erosion originated from slopes, far exceeding debris-flow and landslide initiation slope thresholds. We observed extensive erosion of hillslopes and limited deposition and found that rates of stream channel erosion and deposition are an order of magnitude less than rates of change on hillslopes. We conclude that debris flows are a primary mechanism of sediment export in proglacial basins on Mount Baker.
- Our measurements of gross and net volumetric change in four basins, using DoDs measuring elevation change signals over 4 to 25 years, suggest that erosion rates follow the Pacific Decadal Oscillation (PDO) climate cycles, with colder-wetter periods responsible for greater proglacial erosion.
- Decadal erosion rates in the 0.2–4 mm/yr range found in this study are severalfold greater than millennial rates. While consistent with higher sediment load expectations from stratovolcanoes, our finding may suggest that Mount Baker is in the early (high-erosion) phase of system transition from LIA glacierization to fluvial topography.
- Specific sediment yields (SSYs) in six basins (average 4600 ton/$km^2$/yr) are generally consistent with global measurements in glacierized catchments. In comparing with estimates of SSY downstream of the glacierized catchments, we found that SSY decreased with basin area, despite the presence of glacial sediments in river valleys that undergo secondary remobilization.
- Terrain characteristics explain some variability in proglacial basin sediment yields, with drainage area ($r^2 = 0.82$), hillslope angle ($r^2 = 0.52$), and nonigneous surface lithology fraction ($r^2 = 0.54$) positively correlated; and channel slope ($r^2 = 0.67$) negatively correlated with annualized sediment yield.
- Differences in topography between high and low yielding basins and interactions between the predictive variables indicate that volcanic and Pleistocene glacial history and the resulting spatial distribution of rock type are important in controlling inter-basin variability in erosion rates.
- An empirical power-law model for sediment yield incorporating drainage area and hillslope gradient of the form $Q_s = 2516\, A^{1.44} S_h^{0.68}$ performs well (NSE = 0.86), as does a power law model incorporating only drainage area, $Q = 718\, A^{1.8}$ (NSE = 0.82).
- Our estimates of contributions to riverine total load by glacierized headwater basins range from 11 to 59 % in the North and Middle forks and 18 to 32 % in the main stem Nooksack River, underscoring

the potential for proglacial sediments to influence bed aggradation downstream.

## Declaration of competing interest

The authors declare that they have no known competing financial interests or personal relationships that could have appeared to influence the work reported in this paper.

## Data availability

All data utilized in this study are available upon request.

## Acknowledgements

This research was supported by the NSF PREEVENTS program (Award: ICER 1663859). The authors thank Shelby Ahrendt, Jeff Keck, and Shashank Bhushan for discussions that contributed to the ideas presented in this manuscript.

## Appendix A. Supplementary data

Supplementary data to this article can be found online at https://doi.org/10.1016/j.geomorph.2023.108805.

## References

Ahnert, F., 1970. Functional relationships between denudation, relief, and uplift in large, mid-latitude drainage basins. Am. J. Sci. 268.
Ahrendt, S., Horner-Devine, A.R., Collins, B.D., Morgan, J.A., Istanbulluoglu, E., 2022. Channel Conveyance Variability can Influence Flood Risk as much as Streamflow Variability in Western Washington State. Water Resour. Res. 58 https://doi.org/10.1029/2021WR031890.
Anderson, S., Pitlick, J., 2014. Using repeat lidar to estimate sediment transport in a steep stream. J. Geophys. Res. Earth Surf. 119, 621–643. https://doi.org/10.1002/2013JF002933.
Anderson, S., Konrad, C., Grossman, E., Curran, C., 2019. Sediment Storage and Transport in the Nooksack River Basin, Northwestern Washington, 2006–15 (Scientific Investigations Report), Scientific Investigations Report. U.S. Geological Survey.
Anderson, S.W., 2019. Uncertainty in quantitative analyses of topographic change: error propagation and the role of thresholding. Earth Surf. Process. Landf. 44, 1015–1033. https://doi.org/10.1002/esp.4551.
Anderson, S.W., Konrad, C.P., 2019. Downstream-propagating channel responses to decadal-scale climate variability in a glaciated river basin. J. Geophys. Res. Earth Surf. 124, 902–919. https://doi.org/10.1029/2018JF004734.
Anderson, S.W., Shean, D., 2022. Spatial and temporal controls on proglacial erosion rates: a comparison of four basins on Mount Rainier, 1960 to 2017. Earth Surf. Process. Landf. 47, 596–617. https://doi.org/10.1002/esp.5274.
Antoniazza, G., Lane, S.N., 2021. Sediment yield over glacial cycles: a conceptual model. Prog. Phys. Geogr. Earth Environ. 45, 842–865. https://doi.org/10.1177/0309133321997292.
Associated press, 2021. Washington county's flood damages could reach $50 million [WWW Document]. PBS NewsHour. URL. https://www.pbs.org/newshour/nation/washington-countys-flood-damages-could-reach-50-million (accessed 11.18.22).
Bartos, M., Itati01, Debbout, R., Huard, D., 2022. mdbartos/pysheds: 0.3.3. https://doi.org/10.5281/ZENODO.6300489.
Betz-Nutz, S., Heckmann, T., Haas, F., Becht, M., 2023. Development of the morphodynamics on Little Ice Age lateral moraines in 10 glacier forefields of the Eastern Alps since the 1950s. Earth Surf. Dyn. 11, 203–226. https://doi.org/10.5194/esurf-11-203-2023.
Bogen, J., 2008. The Impact of Climate Change on Glacial Sediment Delivery to Rivers.
Burki, V., Hansen, L., Fredin, O., Andersen, T.A., Beylich, A.A., Jaboyedoff, M., Larsen, E., Tønnesen, J.-F., 2010. Little Ice Age advance and retreat sediment budgets for an outlet glacier in western Norway. Boreas. https://doi.org/10.1111/j.1502-3885.2009.00133.x.
Carrivick, J.L., Heckmann, T., 2017. Short-term geomorphological evolution of proglacial systems. Geomorphology 287, 3–28. https://doi.org/10.1016/j.geomorph.2017.01.037.
Carrivick, J.L., Rushmer, E.L., 2009. Inter- and intra-catchment variations in proglacial geomorphology: an example from Franz Josef Glacier and Fox Glacier, New Zealand. Arct. Antarct. Alp. Res. 41, 18–36. https://doi.org/10.1657/1523-0430-41.1.18.
Carrivick, J.L., Tweed, F.S., 2021. Deglaciation controls on sediment yield: Towards capturing spatio-temporal variability. Earth Sci. Rev. 221, 103809. https://doi.org/10.1016/j.earscirev.2021.103809.
Church, M., Slaymaker, O., 1989. Disequilibrium of Holocene sediment yield in glaciated British Columbia. Nature 337, 452–454. https://doi.org/10.1038/337452a0.
Cody, E., Anderson, B.M., McColl, S.T., Fuller, I.C., Purdie, H.L., 2020. Paraglacial adjustment of sediment slopes during and immediately after glacial debuttressing. Geomorphology 371, 107411. https://doi.org/10.1016/j.geomorph.2020.107411.
Curry, A.M., Sands, T.B., Porter, P.R., 2009. Geotechnical controls on a steep lateral moraine undergoing paraglacial slope adjustment. SP 320, 181–197. https://doi.org/10.1144/SP320.12.
Czuba, J.A., et al., 2012. Changes in Sediment Volume in Alder Lake, Nisqually River Basin, Washington, 1945–2011 (Open-File Report), Open-File Report.
Dalton, R., 2021. British Columbia floods to cause $2bn economic loss: Aon [WWW Document]. Insurance Insider. URL. https://www.insuranceinsider.com/article/29gkbiyimu2ar03595jpc/british-columbia-floods-to-cause-2bn-economic-loss-aon (accessed 11.18.22).
Dick, K., 2013. Glacier Change in the North Cascades, Washington: 1900–2009. Portland State University. https://doi.org/10.15760/etd.1062.
Dietrich, W.E., Bellugi, D.G., Sklar, L.S., Stock, J.D., Heimsath, A.M., Roering, J.J., 2013. Geomorphic transport laws for predicting landscape form and dynamics. In: Wilcock, P.R., Iverson, R.M. (Eds.), Geophysical Monograph Series. American Geophysical Union, Washington, D. C, pp. 103–132. https://doi.org/10.1029/135GM09.
Earth Resources Observation and Science (EROS) Center, 2017. Aerial Photography Single Frame. https://doi.org/10.5066/F7610XKM.
Elverhøi, A., Hooke, R.LeB, Solheim, A., 1998. Late Cenozoic erosion and sediment yield from the Svalbard–Barents sea region: implications for understanding erosion of glacierized basins. Quat. Sci. Rev. 17, 209–241. https://doi.org/10.1016/S0277-3791(97)00070-X.
Frans, C., Istanbulluoglu, E., Lettenmaier, D.P., Fountain, A.G., Riedel, J., 2018. Glacier recession and the response of summer streamflow in the Pacific Northwest United States, 1960–2099. Water Resour. Res. 54, 6202–6225. https://doi.org/10.1029/2017WR021764.
Fuller, S.R., 1980. Neoglaciation of Avalanche Gorge and the Middle Fork Nooksack River Valley Mt. Baker, Washington. Western Washington University.
Harper, J.T., 1993. Glacier terminus fluctuations on Mount Baker, Washington, U.S.A., 1940–1990, and climatic variations. Arct. Alp. Res. 25, 332. https://doi.org/10.2307/1551916.
Hasholt, B., Walling, D.E., Owens, P.N., 2000. Sedimentation in arctic proglacial lakes: Mittivakkat Glacier, south-east Greenland. Hydrol. Process. 14, 679–699. https://doi.org/10.1002/(SICI)1099-1085(200003)14:4<679::AID-HYP966>3.0.CO;2-E.
Henck, A.C., Huntington, K.W., Stone, J.O., Montgomery, D.R., Hallet, B., 2011. Spatial controls on erosion in the Three Rivers Region, southeastern Tibet and southwestern China. Earth Planet. Sci. Lett. 303, 71–83. https://doi.org/10.1016/j.epsl.2010.12.038.
Hinderer, M., Kastowski, M., Kamelger, A., Bartolini, C., Schlunegger, F., 2013. River loads and modern denudation of the Alps — a review. Earth Sci. Rev. 118, 11–44. https://doi.org/10.1016/j.earscirev.2013.01.001.
Holm, K., Bovis, M., Jakob, M., 2004. The landslide response of alpine basins to post-Little Ice Age glacial thinning and retreat in southwestern British Columbia. Geomorphology 57, 201–216. https://doi.org/10.1016/S0169-555X(03)00103-X.
Horn, B.K.P., 1981. Hill shading and the reflectance map. Proc. IEEE 69, 14–47. https://doi.org/10.1109/PROC.1981.11918.
Hugonnet, R., McNabb, R., Berthier, E., Menounos, B., Nuth, C., Girod, L., Farinotti, D., Huss, M., Dussaillant, I., Brun, F., Kääb, A., 2021. Accelerated global glacier mass loss in the early twenty-first century. Nature 592, 726–731. https://doi.org/10.1038/s41586-021-03436-z.
Humlum, O., 2000. The geomorphic significance of rock glaciers: estimates of rock glacier debris volumes and headwall recession rates in West Greenland. Geomorphology 35, 41–67. https://doi.org/10.1016/S0169-555X(00)00022-2.
Hyde, J., Crandell, D., 1978. Postglacial Volcanic Deposits at Mount Baker, Washington, and Potential Hazards From Future Eruptions, Professional Paper. USGS.
Istanbulluoglu, E., 2009. Modeling catchment evolution: from decoding geomorphic processes signatures toward predicting impacts of climate change: modeling catchment evolution. Geogr. Compass 3, 1125–1150. https://doi.org/10.1111/j.1749-8198.2009.00228.x.
Istanbulluoglu, E., Tarboton, D.G., Pack, R.T., Luce, C., 2003. A sediment transport model for incision of gullies on steep topography: a transport model for incision of gullies. Water Resour. Res. 39 https://doi.org/10.1029/2002WR001467.
Klein, D., Johnson, G., 1983. Density, Porosity, and Magnetic Properties of Rock Specimens From Southwestern Arizona (Open-file Report), Open-File Report. U.S. Geological Survey.
Knuth, F., Schwat, E., Shean, D., McNeil, C., 2021a. Historical Image Pre-processing (HIPP) pre-release v0.1. https://doi.org/10.5281/ZENODO.5510876.
Knuth, F., Schwat, E., Shean, D., Bhushan, Shashank, Alexandrov, O., 2021b. Historical Structure From Motion (HSfM) Pre-release v0.1. https://doi.org/10.5281/ZENODO.5510870.
Knuth, F., Shean, D., Bhushan, S., Schwat, E., Alexandrov, O., McNeil, C., Dehecq, A., Florentine, C., O'Neel, S., 2023. Historical structure from motion (HSfM): automated processing of historical aerial photographs for long-term topographic change analysis. Remote Sens. Environ. 285, 113379. https://doi.org/10.1016/j.rse.2022.113379.
Koppes, M., Hallet, B., 2006. Erosion rates during rapid deglaciation in Icy Bay, Alaska. J. Geophys. Res. 111, F02023 https://doi.org/10.1029/2005JF000349.
Koppes, M.N., Montgomery, D.R., 2009. The relative efficacy of fluvial and glacial erosion over modern to orogenic timescales. Nat. Geosci. 2, 644–647. https://doi.org/10.1038/ngeo616.
Lancaster, S.T., Nolin, A.W., Copeland, E.A., Grant, G.E., 2012. Periglacial debris-flow initiation and susceptibility and glacier recession from imagery, airborne LiDAR, and

ground-based mapping. Geosphere 8, 417–430. https://doi.org/10.1130/GES00713.1.
Lane, S.N., Bakker, M., Gabbud, C., Micheletti, N., Saugy, J.-N., 2017. Sediment export, transient landscape response and catchment-scale connectivity following rapid climate warming and Alpine glacier recession. Geomorphology 277, 210–227. https://doi.org/10.1016/j.geomorph.2016.02.015.
Legg, N.T., Meigs, A.J., Grant, G.E., Kennard, P., 2014. Debris flow initiation in proglacial gullies on Mount Rainier, Washington. Geomorphology 226, 249–260. https://doi.org/10.1016/j.geomorph.2014.08.003.
Mancini, D., Lane, S.N., 2020. Changes in sediment connectivity following glacial debuttressing in an Alpine valley system. Geomorphology 352, 106987. https://doi.org/10.1016/j.geomorph.2019.106987.
Micheletti, N., Lambiel, C., Lane, S.N., 2015. Investigating decadal-scale geomorphic dynamics in an alpine mountain setting. J. Geophys. Res. Earth Surf. 120, 2155–2175. https://doi.org/10.1002/2015JF003656.
Montgomery, D.R., Brandon, M.T., 2002. Topographic controls on erosion rates in tectonically active mountain ranges. Earth Planet. Sci. Lett. 201, 481–489. https://doi.org/10.1016/S0012-821X(02)00725-2.
Moon, S., Page Chamberlain, C., Blisniuk, K., Levine, N., Rood, D.H., Hilley, G.E., 2011. Climatic control of denudation in the deglaciated landscape of the Washington Cascades. Nat. Geosci. 4, 469–473. https://doi.org/10.1038/ngeo1159.
Nolan, D.M., Post, A.S., Hauer, W., Zinck, A., O'Neel, S., 2017. Photogrammetric Scans of Aerial Photographs of North American Glaciers. https://doi.org/10.18739/A2VH5CJ8K.
Pelto, M., Brown, C., 2012. Mass balance loss of Mount Baker, Washington glaciers 1990–2010: mass balance loss of Mount Baker, Washington glaciers. Hydrol. Process. 26, 2601–2607. https://doi.org/10.1002/hyp.9453.
Pfeiffer, A.M., Collins, B.D., Anderson, S.W., Montgomery, D.R., Istanbulluoglu, E., 2019. River bed elevation variability reflects sediment supply, rather than peak flows, in the uplands of Washington State. Water Resour. Res. 55, 6795–6810. https://doi.org/10.1029/2019WR025394.
Portenga, E.W., Bierman, P.R., 2011. Understanding Earth's eroding surface with 10Be. GSAT 21, 4–10. https://doi.org/10.1130/G111A.1.
Post, A., 1995. Annual aerial photography of glaciers in northwest North America: how it all began and its Golden Age. Phys. Geogr. 16, 15–26. https://doi.org/10.1080/02723646.1995.10642540.
Post, A., Richardson, D., Tangborn, W., Rosselot, F.L., 1971. Inventory of Glaciers in the North Cascades, Washington (Paper), Professional Paper. U.S. Geological Survey.
Prancevic, J.P., Lamb, M.P., Fuller, B.M., 2014. Incipient sediment motion across the river to debris-flow transition. Geology 42, 191–194. https://doi.org/10.1130/G34927.1.
PRISM Climate Group, 2014. Oregon State University [WWW Document]. URL. https://prism.oregonstate.edu (accessed 12.12.22).
Reiners, P.W., Ehlers, T.A., Garver, J.I., Mitchell, S.G., Montgomery, D.R., Vance, J.A., Nicolescu, S., 2002. Late Miocene exhumation and uplift of the Washington Cascade Range. Geol 30, 767. https://doi.org/10.1130/0091-7613(2002)030<0767:LMEAUO>2.0.CO;2.
Reiners, P.W., Ehlers, T.A., Mitchell, S.G., Montgomery, D.R., 2003. Coupled spatial variations in precipitation and long-term erosion rates across the Washington Cascades. Nature 426, 645–647. https://doi.org/10.1038/nature02111.
RGI Consortium, 2017. Randolph Glacier Inventory - A Dataset of Global Glacier Outlines, Version 6. https://doi.org/10.7265/4M1F-GD79.
Roe, G.H., O'Neal, M.A., 2009. The response of glaciers to intrinsic climate variability: observations and models of late-Holocene variations in the Pacific Northwest. J. Glaciol. 55, 839–854. https://doi.org/10.3189/002214309790152438.
Rolstad, C., Haug, T., Denby, B., 2009. Spatially integrated geodetic glacier mass balance and its uncertainty based on geostatistical analysis: application to the western Svartisen ice cap, Norway. J. Glaciol. 55, 666–680. https://doi.org/10.3189/002214309789470950.
Scott, D.N., Collins, B.D., 2021. Frequent mass movements from glacial and lahar terraces, controlled by both hillslope characteristics and fluvial erosion, are an important sediment source to Puget Sound Rivers. Water Res. 57 https://doi.org/10.1029/2020WR028389.
Scott, K., Tucker, D., Riedel, J., Gardner, C., McGeehin, J., 2020. Latest Pleistocene to Present Geology of Mount Baker Volcano, Northern Cascade Range, Washington (Scientific Investigations Report), Professional Paper. U.S. Geological Survey.
Slater, L.J., Singer, M.B., Kirchner, J.W., 2015. Hydrologic versus geomorphic drivers of trends in flood hazard. Geophys. Res. Lett. 42, 370–376. https://doi.org/10.1002/2014GL062482.
Slaymaker, O., 2018. A global perspective on denudation data, primarily specific sediment yield in mountainous regions. Landf. Anal. 36, 19–31. https://doi.org/10.12657/landfana.036.003.
Strauch, R., Istanbulluoglu, E., Nudurupati, S.S., Bandaragoda, C., Gasparini, N.M., Tucker, G.E., 2018. A hydroclimatological approach to predicting regional landslide probability using Landlab. Earth Surf. Dyn. 6, 49–75. https://doi.org/10.5194/esurf-6-49-2018.
Tabor, R.W., Haugerud, R.A., Hildreth, W., Brown, E.H., 2003. Geologic Map of the Mount Baker 30- by 60-Minute Quadrangle, Washington.
Takahashi, T., 1978. Mechanical characteristics of debris flow. J. Hydraul. Div. 104, 1153–1169. https://doi.org/10.1061/JYCEAJ.0005046.
Tucker, D.S., Scott, K.M., Grossman, E.E., Linneman, S., 2014. Mount Baker lahars and debris flows, ancient, modern, and future. In: GSA Field Guides, pp. 33–52. https://doi.org/10.1130/2014.0038(03).
Turowski, J.M., Rickenmann, D., Dadson, S.J., 2010. The partitioning of the total sediment load of a river into suspended load and bedload: a review of empirical data: the partitioning of sediment load. Sedimentology 57, 1126–1146. https://doi.org/10.1111/j.1365-3091.2009.01140.x.
U.S. Geological Survey, 2019. The StreamStats Program.
Virtanen, P., et al., 2020. SciPy 1.0: fundamental algorithms for scientific computing in Python. Nat. Methods 17, 261–272. https://doi.org/10.1038/s41592-019-0686-2.
Werner, C., Evans, W.C., Poland, M., Tucker, D.S., Doukas, M.P., 2009. Long-term changes in quiescent degassing at Mount Baker Volcano, Washington, USA; evidence for a stalled intrusion in 1975 and connection to a deep magma source. J. Volcanol. Geotherm. Res. 186, 379–386. https://doi.org/10.1016/j.jvolgeores.2009.07.006.
Wood, C.A., Kienle, Juergen, 1990. Volcanoes of North America: United States and Canada, 1. Paperback. Cambridge Univ. Pr, New York.
Xdem Contributors, 2021. xdem. https://doi.org/10.5281/ZENODO.4809698.
Zemp, M., Frey, H., Gärtner-Roer, I., Nussbaumer, S.U., Hoelzle, M., Paul, F., Haeberli, W., Denzinger, F., Ahlstrøm, A.P., Anderson, B., Bajracharya, S., Baroni, C., Braun, L.N., Cáceres, B.E., Casassa, G., Cobos, G., Dávila, L.R., Delgado Granados, H., Demuth, M.N., Espizua, L., Fischer, A., Fujita, K., Gadek, B., Ghazanfar, A., Ove Hagen, J., Holmlund, P., Karimi, N., Li, Z., Pelto, M., Pitte, P., Popovnin, V.V., Portocarrero, C.A., Prinz, R., Sangewar, C.V., Severskiy, I., Sigurđsson, O., Soruco, A., Usubaliev, R., Vincent, C., 2015. Historically unprecedented global glacier decline in the early 21st century. J. Glaciol. 61, 745–762. https://doi.org/10.3189/2015JoG15J017.